



Contents lists available at ScienceDirect

International Journal of Biological Macromolecules

journal homepage: www.elsevier.com/locate/ijbiomac

Synthesis of oxidized sodium alginate and its electrospun bio-hybrids with zinc oxide nanoparticles to promote wound healing

Wei Wang^{a,1}, MingYue Liu^{a,1}, Muhammad Shafiq^{a,b,*}, HaiYan Li^a, Rashida Hashim^c, Mohamed EL-Newehy^d, Hany EL-Hamshary^d, Yosry Morsi^e, Xiumei Mo^{a,**}

^a State Key Laboratory for Modification of Chemical Fibers and Polymer Materials, Shanghai Engineering Research Center of Nano-Biomaterials and Regenerative Medicine, College of Biological Science and Medical Engineering, Donghua University, Shanghai, 201620, China

^b Department of Chemical Engineering, Faculty of Chemical Engineering, Graduate School, Kyushu University, 744 Motoooka, Nishi-ku, Fukuoka, Japan

^c School of Physical Sciences, University of Punjab (PU), Lahore 54000, Pakistan

^d Department of Chemistry, College of Science, King Saud University, P.O. Box 2455, Riyadh 11451, Saudi Arabia

^e Faculty of Engineering and Industrial Sciences, Swinburne University of Technology, Boroondara, VIC 3122, Australia

ARTICLE INFO

Keywords:

Sodium alginate
Electrospinning
Wound dressing
ZnO-NPs
Tissue engineering
Functionalization

ABSTRACT

Electrospun fibers provide a promising platform for wound healing; however, they lack requisite characteristics for wound repair, including antibacterial and anti-inflammatory properties and angiogenic ability. Sodium alginate (SA) is being used for different types of applications. However, the poor spinnability of SA restricts its applications. The objectives of this study were three-fold: a) to synthesize oxidized sodium alginate (OSA) to improve its spinnability, b) to fabricate composite fibrous membranes by blending OSA along with zinc oxide nanoparticles (ZnO-NPs), and c) to decipher antibacterial and anti-inflammatory properties as well as biocompatibility of membranes *in vitro* and *in vivo*. OSA displaying different oxidation degrees (Dox (%)) was synthesized by varying the molar ratio of sodium periodate to SA. OSA (Dox, ~48 %) afforded smooth and uniform fibers; 0.5 wt% of adipic dihydrazide (ADH) evolved into structurally stable and water-insoluble membranes. Composite fibrous membranes containing 2 wt% of ZnO-NPs displayed good biocompatibility and bactericidal effect against *Escherichia coli* (*E. coli*) and *Staphylococcus aureus* (*S. aureus*) *in vitro*. In addition, composite membranes showed remarkable epithelialization, neovascularization, and anti-inflammatory response than that of the membranes devoid of ZnO-NPs. Conclusively, these composite fibrous membranes may have broad implications for wound healing applications.

1. Introduction

The skin being the largest organ of the human body plays a pivotal role in homeostasis. Upon tissue insult or an injury, skin tissues undergo different stages of wound healing, including hemostasis, inflammation, proliferation, and remodeling [1]. The disruption in any of these stages may prolong the healing process. Of different reasons which may drive an acute wound into a chronic non-healing wound, infection is the most deleterious, which becomes further severe in diabetic patients [2]. A series of strategies has been applied to overcome infection, including the application of therapeutics, antibacterial agents, and photodynamic

therapy (PDT) [3,4]. Inorganic nanomaterials (NMs), such as zinc oxide nanoparticles (ZnO-NPs) have been shown to be promising antibacterial agents against different types of bacterial species. Antibacterial activity of ZnO-NPs may be ascribed to their interaction with the bacterial cell wall as well as their capability to aggravate oxidative stress through the production of reactive oxygen species (ROS). Besides, wound dressings should display certain characteristics, such as extracellular matrix (ECM)-mimetic morphological features, moistness, and appropriate porosity for the diffusion of oxygen and the transport of nutrients [5,6].

Until now, different types of materials have been used for the fabrication of wound dressings, such as natural polymers, synthetic

* Correspondence to: M. Shafiq, Department of Chemical Engineering, Faculty of Chemical Engineering, Graduate School, Kyushu University, 744 Motoooka, Nishi-ku, Fukuoka, Japan.

** Corresponding author.

E-mail addresses: shafiqdr786@yahoo.com (M. Shafiq), xmm@dhu.edu.cn (X. Mo).

¹ These authors contributed equally to this work.

<https://doi.org/10.1016/j.ijbiomac.2023.123480>

Received 9 June 2022; Received in revised form 22 January 2023; Accepted 26 January 2023

Available online 28 January 2023

0141-8130/© 2023 Elsevier B.V. All rights reserved.

polymers, bioactive glasses (BGs), and organic/inorganic hybrids. While synthetic biodegradable polymers are easy to be synthesized and manipulated in terms of their mechanical properties and degradation profiles, they lack cell recognition moieties and necessitate functionalization with ECM proteins or ECM-derived peptides [7]. On the other hand, while natural polymers better mimic tissue microenvironment and display biocompatibility, they show rapid degradation and weak mechanical properties, which may hamper their applicability. Similarly, while different types of methods can be used for the fabrication of wound dressings, such as freeze drying, salt leaching, and electrospinning, it is only the latter which may afford ECM-mimetic microenvironment [8,9]. Physical properties, including fiber diameter, fibers' alignment, pore size, and porosity of electrospun scaffolds can be tailored to afford a range of scaffolds with distinct morphological features and properties. Moreover, different types of electrospinning techniques can be employed to further tailor the abovementioned physical properties as well as incorporate different types of bioactive cues for a better therapeutic effect [10,11]. Bioactive cues or NMs can be either directly encapsulated into fibers or immobilized onto scaffolds to further widen their applicability for wound repair [12–15].

Sodium alginate (SA) is a natural polysaccharide derived from brown algae and has been shown to possess good cytocompatibility and non-immunogenicity [16,17]. Owing to the remarkable characteristics of SA, including good water solubility and calcium ions (Ca^{2+})-triggered gelation, it has been widely explored for an array of applications, including food preservation, bioremediation, and drug delivery systems (DDS). Moreover, SA can be fabricated into different shapes and structures, such as nanoparticles (NPs), hydrogels, microspheres, films, and fibers [18,19]. SA and glycosaminoglycans (GAGs) possess similar characteristics. Electrospun SA fibers recapitulate ECM-like morphological features, which may provide a conducive environment for cell adhesion, growth, and differentiation for better tissue regeneration [17,20]. Despite abovementioned merits, poor spinnability of the aqueous solution of SA presumably due to its multi-electrolyte nature, lack of chain entanglement due to the rigidity of polysaccharide molecular chains, and strong cohesive forces among polyanions hampers its applicability [21].

The poor spinnability of SA has been partly improved by blending it along with other polymers, such as polyethylene oxide (PEO) and poly(vinyl alcohol) (PVA). However these approaches require additional steps for the complete removal of the additional components after electrospinning. Alternatively, certain molecules, such as glycerol, which exhibit hydroxyl ($-\text{OH}$) groups, can be mixed with alginate to weaken hydrogen bonding among polymer chains. The weakening of the hydrogen-bonding among alginate chains may improve chain entanglement, thereby improving the spinnability. Another approach to

weaken inter/intra-molecular hydrogen bonding of the SA involves the opening of the uronate rings. The ring-opening of molecular chains can improve their flexibility, weaken strong intramolecular hydrogen bonding, and improve spinnability [22]. Oxidized sodium alginate (OSA) is generally prepared by using periodic acid, which disrupts the linkage between the C-2 and C-3 bonds of uronic acid units, thereby evolving into a dialdehyde group (Fig. 1). Consequently, OSA shows lower viscosity and good water solubility than that of the SA. Due to the high activity of dialdehyde groups and good biocompatibility, OSA has been widely exploited to fabricate films, hydrogels, and beads for tissue engineering (TE) applications [23,24]. However, electrospinning of OSA, especially for biomedical applications has rarely been reported [24].

Recently, a series of organic-inorganic hybrids has been leveraged for soft and hard tissue repair applications [25]. Different types of NPs manifesting promising therapeutic effects have been incorporated into electrospun fibers. ZnO-NPs have been shown to exhibit antibacterial and anti-inflammatory properties [26]. Besides, zinc (Zn) has been shown to promote wound healing by resolving inflammatory response as well as improving epithelialization, neovascularization, and tissue regeneration [27]. ZnO-NPs may exert antibacterial effects through multiple mechanisms, such as by directly interacting with the bacterial cell wall or by releasing zinc ions (Zn^{2+}) for ROS production [28–31]. In addition, ZnO-NPs have also been incorporated into fibers to afford antibacterial wound dressings. Castellano et al. [32] fabricated alginate-based fibers containing ZnO-NPs, which enabled sufficient cell adhesion and growth, low protein adsorption, negligible bacterial cell adhesion, and good water vapor permeability. Nonetheless, the minimum stability of ionically-crosslinked fibers, especially, those crosslinked with the Ca^{2+} as well as lack of *in vivo* results of abovementioned membranes justify further investigations. The minimum stability of Ca^{2+} -crosslinked fibers may be ascribed to the exchange of Na^{+} in the solution with Ca^{2+} bound to carboxylates in the alginate chains [32].

As mentioned above, while ZnO-NPs can be blended along with the SA by using carrier polymers, such as PEO and PVA, additional steps may be required for the complete removal of the sacrificial polymers for biomedical applications. Moreover, to further widen the electrospinning of SA and afford a robust method for the chemical crosslinking and stabilization of scaffold materials, oxidized derivatives of SA may hold great technological prospects. Oxidized derivatives of SA may not only help improve the spinnability of SA owing to decreased intra/intra-molecular hydrogen bonding, low viscosity, and better chain entanglements, but may also help tailor the biodegradability of scaffolds and crosslinking/blending with other polymers due to a variety of functional groups on oxidized alginate chains.

Therefore, objectives of this study were three-fold: (1) to optimize

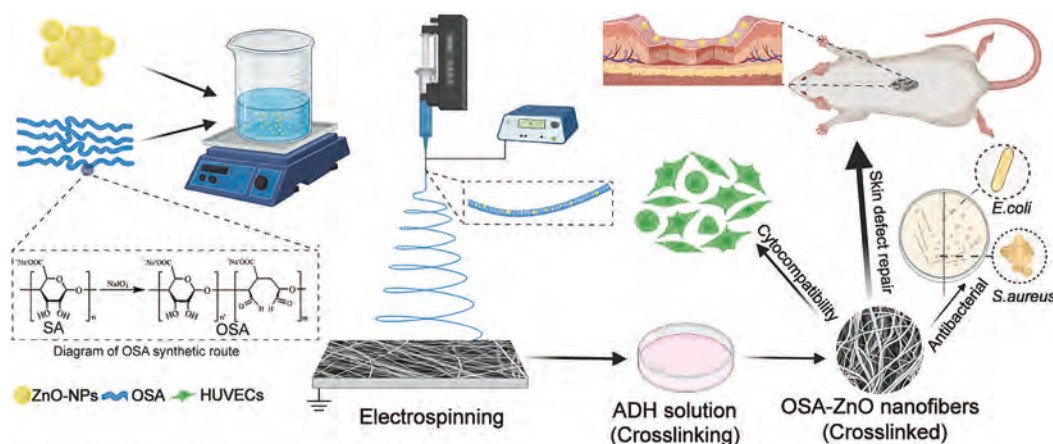


Fig. 1. Schematic illustration showing the preparation of oxidized sodium alginate (OSA), OSA/ZnO-NPs based composite nanofibrous membranes and their *in vitro* and *in vivo* evaluation for wound healing applications.

synthesis conditions of OSA to improve the spinnability of SA, (2) to fabricate OSA/ZnO-NPs-based composite fibrous dressings, and (3) to assess the potential of these dressings for skin repair *in vitro* and *in vivo* (Fig. 1). The OSA with different oxidation degrees (Dox (%)) was prepared, electrospun, and chemically-crosslinked with adipic acid dihydrazide (ADH) to afford water-insoluble fibrous membranes. OSA with a Dox (%) value of 48 % afforded smooth and uniform fibers, which was further leveraged to design bio-hybrids with ZnO-NPs. A series of evaluations, such as physicochemical properties, cytocompatibility, antibacterial properties, and *in vivo* wound healing was carried out.

2. Materials and methods

2.1. Materials

Sodium alginate (M_w , 250 kDa and M/G fragment ratio, 0.54) was purchased from Qingdao Mingyue group, Qingdao, China. Dialysis tubes (cut off $M_w = 7000$ – $14,000$ Da) were obtained from Solarbio Chemical Reagent Company (Beijing, China). Triton X-100, PEO ($M_w = 5000$ kDa), and ADH ($M_w = 174.2$ g/mol) were purchased from Macklin Biochemical Co., Ltd. (Shanghai, China). ZnO-NPs (product #, Z112849 and diameter, 50 ± 10 nm) were purchased from Shanghai Aladdin Bio-Chem Technology Co., Ltd. (Shanghai, China). Other chemicals and reagents, such as sodium periodate (NaIO_4), ethylene glycol, ethanol, hydrochloric acid (HCl), and sodium hydroxide (NaOH) were purchased from Sinopharm Chemical Reagent Co., Ltd. (Shanghai, China). All materials were used directly without any further purification. Distilled water was used throughout the experiments.

2.2. Preparation of oxidized sodium alginate

The OSA was prepared by following a previous report with slight modification [24]. Briefly, SA (5 g) was dispersed in 100 mL of ethanol. Varying content of NaIO_4 were dropwise added into 100 mL of water and the mixture was stirred at room temperature while being protected from the light to obtain OSA with different Dox (%). The amount of NaIO_4 depends upon the required molar ratio of NaIO_4 to the number of repetitive units of the SA ($n(\text{NaIO}_4) : n(\text{SA}) = x$), where x denotes 0.6, 0.7, 0.8, 1.0, 1.2, and 1.5. After 4 h of reaction, an equal amount of ethylene glycol was added to the solution to terminate the reaction. The precipitates were collected by centrifugation and resuspended in distilled water. The mixture was transferred to a dialysis bag and purified for up to three days against an excess amount of deionized water and freeze-dried to obtain the final product.

2.3. Characterization of oxidation products

2.3.1. Determination of oxidation degree

The degree of oxidation (Dox (%)) of OSA was defined as the molar ratio of the oxidized ring-opened glycoaldehyde residues to total residues ($M + G$) of SA and determined by hydroxylamine hydrochloride/NaOH potentiometric titration method [33,34]. Briefly, hydroxylamine hydrochloride (15 g) was dissolved in 30-mL of deionized water. Thereafter, 40-mL of ethanol (anhydrous), 100-mL of NaOH solution (4.2 %, w/v), and 5-mL of bromophenol blue solution (0.45 %, w/v) were added into hydroxylamine solution and the mixture was stirred at ambient temperature overnight. The supernatant was separated for subsequent use. Then the HCl solution was configured and its exact concentration was calibrated as " N " (mol/L). Finally, 5-mL of hydroxylamine hydrochloride solution and 5-mL of anhydrous ethanol solution were slowly heated, refluxed for up to 40 min, and cooled for up to room temperature. This solution was titrated against calibrated HCl solution until the purple colour of hydroxylamine hydrochloride solution was turned into yellowish green colour; the used volume of the HCl was recorded for blank experimental correction. Appropriate amount of SA was weighed and dissolved into a mixture solution composed of 5-mL of

hydroxylamine hydrochloride and 5 mL of anhydrous ethanol. The above titration steps were repeated and the consumed volume of HCl was recorded to calculate the Dox (%) by Eq. (1):

$$\text{Dox (\%)} = (M \times N (V_{\text{control}} - V_{\text{sample}}) / 2m) \times 100 \quad (1)$$

where M , N , and m represent the M_w of SA repeating unit (g/mol), exact concentration of the HCl solution (mol/L), and the mass of SA, respectively. The V_{control} and V_{sample} indicate the consumed volume of the HCl by the blank and samples, respectively. The reported values for the OD (%) were an average of four samples.

2.3.2. Structural analysis

Structural analysis of SA and OSA with three Dox (%) was performed by Fourier-transform infrared spectroscopy (FTIR, Nicolet-760, Thermo-Fisher Scientific, Madison, WI) and nuclear magnetic resonance spectroscopy (NMR, Bruker 400 MHz NMR spectrometer, Bruker, Switzerland). FTIR spectrophotometer was used in the range of 4000 – 500 cm^{-1} . For NMR, SA and 1.0-OSA were dissolved in deuterated water at a concentration of 15 mg/mL. The ^1H NMR spectra of samples were collected by using NMR at 80 °C with 24 and 50,000 scan numbers.

2.4. Preparation of oxidized sodium alginate fibers

2.4.1. Preparation of sodium alginate solution

The OSA synthesized by using varying molar ratios of NaIO_4 to the number of repetitive units of SA (0.6, 0.8 and 1.0 labeled as 0.6-OSA, 0.8-OSA, and 1.0-OSA, respectively), was dissolved in deionized water at room temperature to afford 15 % (w/v) solution. Thereafter, PEO (0.5 %, w/v), Triton X-100 (0.8 %, w/v), and ethanol (10 %, w/v) were added into the OSA solution.

2.4.2. Preparation of oxidized sodium alginate/ZnO-NPs solution

The OSA with an appropriate Dox (~ 48 %) was next blended along with ZnO-NPs. The OSA solution was prepared as detailed in the Section 2.4.1. Thereafter, ZnO-NPs (1%, 2%, and 3% (w/w) with respect to the OSA) were dispersed in the OSA solution. OSA membranes devoid of ZnO-NPs acted as a control group. It is noteworthy to mention here that these particular concentrations of ZnO-NPs were chosen based on our preliminary antibacterial and cytotoxicity studies [26,27].

2.4.3. Electrospinning of oxidized sodium alginate-based nanofibers

Once ultrasonicated for 15 min, about 10-mL of solution was loaded into a plastic syringe equipped with a 22-gauge needle. Following electrospinning parameters were used for the fabrication of OSA and OSA/ZnO-NPs based fibers: flow rate, 0.8 mL/h; voltage, 18 kV; collector speed, 120 rotations per minute (rpm); and distance from the spinneret to the collector, 15-cm. The temperature and humidity were approximately 25 °C and 50%, respectively. Fibers prepared from OSA displaying three Dox (%) were named as OSA-0.6, OSA-0.8 and OSA-1.0. On the other hand, fibers containing ZnO-NPs were named as OZ-1, OZ-2 and OZ-3 indicating 1, 2, and 3 wt% of ZnO-NPs, respectively. Membranes prepared with OSA solution without ZnO-NPs were named as OF and were used as a control group. After electrospinning, membranes were dried in a fume hood and crosslinked with ADH solution; the latter was prepared in ethanol/water mixture (5:2, v/v). Membranes prepared by using OSA with different Dox (%) including 0.6-OSA, 0.8-OSA, and 1.0-OSA were crosslinked by ADH (0.0, 0.05, 0.1, 0.5, and 1.0 wt%) for up to 4 h. On the other hand, composite fibers, including OZ-1, OZ-2, and OZ-3 were crosslinked by using ADH solution (0.5 %, w/v in ethanol/water mixture, 5:2, v/v) for up to 4 h at room temperature to afford insoluble membranes.

2.5. Characterization of fibers

It is worthy to note that generally cations like calcium (Ca^{2+}), barium

(Ba²⁺), and strontium (Sr²⁺) are used to ionically-crosslink alginate-based scaffolds via electrostatic interactions [35]. However, the minimal stability of ionically-crosslinked alginate fibers, especially, those cross-linked with the Ca²⁺ may hamper this approach. The sodium ions (Na⁺) in the solution may be exchanged with the Ca²⁺ bound to carboxylates in the alginate chains, thereby weakening the structural stability [32,35]. Alternatively, covalent crosslinking by ADH has been previously employed to crosslink alginate through well-established carbodiimide chemistry by using water soluble carbodiimide (EDC) as an activator and ADH as a crosslinker [36]. As aldehyde groups of the OSA can react with the amino (—NH₂) groups of the ADH to form relatively stable hydrazone bonds, we employed different content of ADH to crosslink OSA and OSA/ZnO-NPs membranes.

The surface morphology and elemental analysis of electrospun membranes were examined by using a scanning electron microscope (SEM, Phenom XL, Phenom Scientific Instruments Co. Ltd., Shanghai, China) with an Environmental Scanning Electron Microscope (EDS, Quanta250, Czech Republic) at an accelerating voltage of 15-kV. Prior to the SEM, well-dried membranes were sputter-coated with gold for up to 45 s. The diameter of fibers was calculated by using ImageJ software (National Institute of Health, USA); about 100 fibers were measured to ascertain the average diameter.

X-ray diffraction (XRD) patterns were collected to examine the incorporation of ZnO-NPs into membranes as well as assess the crystallinity of composite membranes. Bruker AXS D8 Discover X-ray diffractometer was used to scan the samples from $2\theta = 5^\circ - 60^\circ$.

The OSA membranes prepared with different Dox (%) and cross-linked with the different concentrations of ADH were subjected to *in vitro* degradation for up to 14 days. About 10-mg of membrane samples ($n = 3$ for each time point and for each group) were placed into a centrifuge tube (CP2225D, Precision electronic balance, Germany), sterilized with ultraviolet (UV) light for up to 12 h, and filled with 5-mL of phosphate-buffered saline (PBS) under aseptic conditions. At certain time intervals, membranes were washed with water and dried in a vacuum oven for up to a constant weight. Once weighted after drying, samples were further examined with SEM for morphological analysis. The mass loss of samples was determined by Eq. (2):

$$\text{Remained mass (\%)} = W_t/W_0 \times 100\% \quad (2)$$

where W_0 and W_t indicate the mass of the sample before and after degradation, respectively.

For tensile mechanical properties, rectangular strips ($n = 5$, 10 mm \times 40 mm) were punched from membranes and assessed for dimensions for the subsequent calculation of the cross-sectional area. The specimen was affixed onto a uniaxial tensile tester (HY-940FS, Hyclone, Logan, UT, USA) equipped with a 5 kg load sensor (BAB-20MT, Transcell Technology, Inc., Buffalo Grove, IL, USA) and evaluated at a strain rate of 8 mm/min until failure. Mechanical properties, such as ultimate tensile strength (UTS), elongation at break (Eb), and Young's modulus (E) were measured from stress-strain curves. The E was calculated from the initial 5 % linear slope of the stress-strain curves.

Thermogravimetric analysis (TGA) of 1.0-OSA, OSA-1.0 fibers, and OSA-ZnO composite fibers was performed by using a thermogravimetric analyzer (SQ8-STA8000, PerkinElmer, Waltham, MA, USA). Samples were scanned from 50 °C for up to 800 °C in an inert atmosphere at a scan rate of 10 °C per minute.

2.6. Antibacterial activity

Antibacterial activities of fibers were discerned against two representative bacterial species, including *Staphylococcus aureus* (*S. aureus*, ATCC 25923) and *Escherichia coli* (*E. coli*, ATCC 25922), which were purchased from Chinese Academy of Sciences, Shanghai, China. Both types of bacteria species were cultured overnight in conical jars with Luria-Bertani (LB) broth culture medium (LB Broth Agar, Sangon

Biotech, Shanghai, China) in a shaker (HZQ-X300C, Shanghai bluepard instruments Co., Ltd. Shanghai, China) at 37 °C. Before inoculation of bacteria on the surface of membranes, scaffolds were cut into circular shapes (diameter, 14-mm) and sterilized by using UV irradiation on both sides for up to 12 h. The antibacterial activity of samples was assessed by using an AGAR plate (8211GR500, BioFroxx, Saiguo Biotech Co., Ltd., Guangzhou, China), while the bacterial morphology was examined by using SEM. About 100- μ L of germy inoculum (10^5 CFU/mL) was added into each well in a 24-well plate and incubated overnight at room temperature. At day 2, the same volume of bacterial solution was transferred to PBS, vortexed for 1 min, and diluted to an appropriate concentration. About 100- μ L of bacterial suspension was prepared in PBS and evenly spread on the AGAR plate containing LB medium and cultured for up to 24 h at 37 °C for subsequent imaging and colony counting. Once fixed with 4% paraformaldehyde (PFA), membranes were treated with gradient ethanol series, dried, and evaluated by SEM for morphological analysis. Tissue culture plates (TCPs) were employed as a control group ($n = 3$ for each group). The survival rate of bacteria was calculated by Eq. (3):

$$\text{Normalized survival rate (\%)} = (A_{\text{TCPs}} - A_{\text{test}})/A_{\text{TCP}} \times 100\% \quad (3)$$

where A_{TCPs} and A_{test} indicate the number of colonies on the cell culture plate and the experimental group, respectively.

2.7. Cytocompatibility

We next assessed the cytocompatibility of membranes *in vitro* by using NIH-3T3 fibroblasts and human umbilical vein endothelial cells (HUVECs) (Typical Culture Collection Committee Cell Bank, Chinese Academy of Science, Shanghai, China). Cells were cultured in 89 % Dulbecco's modified Eagle's medium high-glucose supplemented with 1 % of 100 U/mL penicillin, 0.1 mg/mL of streptomycin, and 10% fetal bovine serum (Gibco Life Technologies, Co., Waltham, MA, USA). Cells were cultured in an incubator at 37 °C and 5% CO₂. Membranes were cut into circular shapes (diameter, 14-mm) and sterilized by using UV for up to 12 h on each side. Thereafter, membranes were transferred to the wells of 24-well culture plates and affixed with sterilized stainless steel rings. An automatic cell counter (Countstar, IC1000, China) was used for cell counting before seeding on the membranes. The NIH-3 T3 fibroblasts and HUVECs (1×10^4 cells/well) were seeded on membranes ($n = 4$ for every group) and incubated at 37 °C and 5 % CO₂. The culture medium was changed at an interval of one day.

Cell viability and proliferation was assessed by using live/dead cell assay and cell counting kit (CCK-8) assay; the respective kits were acquired from Yeasen Biotech Co., Ltd., Shanghai, China. For cell proliferation, at day 1, 4, and 7, the culture medium was removed and membranes were washed with PBS for three times. Thereafter, a total 400- μ L of CCK-8/DMEM mixture solution (1:10, v/v) was added into each well and samples were incubated 37 °C and 5 % CO₂ for 2 h. About 200- μ L of the test solution was then transferred to a 96-well plate and the absorbance was measured at 450 nm by using a microplate reader (Thermo Fisher Multiskan FC, Thermo Fisher Scientific, Waltham, MA, USA). For live/dead assay, at day 4, the culture medium was removed and membranes were washed with PBS for three times. Thereafter, about 200- μ L of a calcein AM/propidium iodide (PI) solution in PBS (calcein AM, PI, and PBS were 10- μ L, 1- μ L, and 1000- μ L, respectively) was added to each well. Cells were incubated at 37 °C for 30 min, and then imaged by fluorescence microscope (DMI 8, Leica, Germany) ($n = 3$ for each group).

To gain further insight into the morphology of cells seeded on membranes, at day 4, culture medium was removed and membranes were washed with PBS for three times. Once fixed with 4% PFA at 4 °C for 2 h, membranes were dehydrated by gradient ethanol series, dried at room temperature and sputter-coated with gold. Membranes were observed by SEM (Hitachi, TM-1000, Japan).

2.8. In vivo wound healing

Male Sprague Dawley (SD) rats (weight, 180–200 g, age, 7–8 weeks) were purchased from JSJ Animal Experimental Center, Shanghai, China. Rats were acclimated at 25 °C and 40–70% humidity in an animal house. Surgical operations were performed by following the Guidelines for the care and use of laboratory animals (National Institutes of Health, 8th edition, 2011). The animal experiments were carried out by following the guidelines of the Ethics Committee of Donghua University, Shanghai, China.

2.8.1. Implantation of membranes in vivo

The SD rats were anesthetized by an intramuscular injection of Zolide (40 mg/kg) and 2% Xilazina (3 mg/kg), shaved and treated with 70% ethanol. A circular wound (diameter, 10-mm) was created on the back of SD rats. Membranes were cut into circular shapes (diameter, 14-mm) and sterilized by UV for 12 h on both sides for implantation. The experiment was divided into three groups ($n = 3$ for each group and for each time point). The first group was treated with sterile adhesive dressing (3 M Tegaderm™, MN, USA) as the control group. The second and third groups received OF and OZ-2 membranes, respectively, which were further covered with sterilized adhesive dressing. Wounds were photographed at day 0, 3, 7 and 14, and the area of the wounds was measured with ImageJ software and the percentage of wound area was calculated by Eq. (4):

$$\text{Wound area (\%)} = A_t/A_0 \times 100 \quad (4)$$

where A_0 and A_t represent the average wound area of rats at day 0 and at different time points, respectively.

2.8.2. Analysis of explanted samples

Rats were sacrificed at day 3, 7 and 14 and tissues were collected from the wound surface and surrounding healthy skin for histological and immunohistochemical analysis. Tissues were fixed by using 4% PFA and embedded in paraffin [37]. Tissue sections (thickness, 5 mm) were cut and subjected to hematoxylin–eosin (H&E) and Masson's trichrome (MT) staining. Images were collected by using a digital slide scanner (PRECICE 500×) [38].

Immunohistochemical analysis of retrieved tissue sections was performed by using our previous report with slight modification [39]. Briefly, paraffin-embedded sections were deparaffinized by xylene, dehydrated with gradient ethanol series, and rehydrated for antigen retrieval. After quenching with 3% hydrogen peroxide and blocking with 5% bovine serum albumin (BSA), sections were incubated with primary antibodies, such as anti-CD31 (1:200; Abcam), anti-CD68 (1:500; Abcam), anti-CD86 (1:300, Proteintech), and anti-CD206 (1:1000, Proteintech) at 4 °C overnight. After incubation with biotinylated secondary antibodies, sections were visualized by using Nikon DS-U3 system (Nikon Corporation, Tokyo, Japan). The wound area and average fluorescence intensity of the stained sections were statistically analyzed by using ImageJ software.

2.9. Statistical analysis

Quantitative data were expressed as a mean \pm standard deviation (SD). All data were analyzed by one-way analysis of variance (ANOVA) with Tukey's multiple comparison tests and a value of $p \leq 0.05$ was considered to be statistically significant.

3. Results

3.1. Structural analysis

FTIR spectra were collected for the structural analysis of modified sodium alginate (Fig. 2(A)). Absorption band at 3340 cm^{-1} is ascribed to

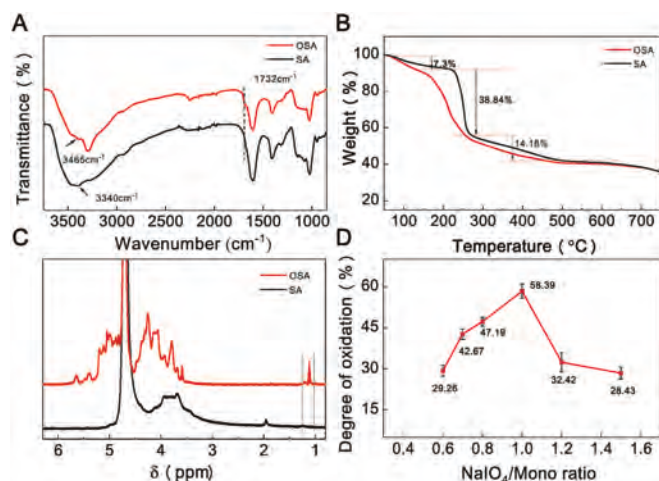


Fig. 2. Structural analysis of sodium alginate and oxidized sodium alginate. FTIR spectra of SA and 1.0-OSA (A), TGA thermograms of SA and 1.0-OSA (B), ^1H NMR spectra of SA and 1.0-OSA (C), and Dox (%) of OSA prepared as a function of the molar ratio of NaIO_4 /sodium alginate (D).

the hydroxyl ($-\text{OH}$) groups of SA. Due to oxidation, the degree of hydroxyl groups of SA was decreased; the peak attributed to the hydroxyl ($-\text{OH}$) groups was shifted toward higher wave number (3465 cm^{-1}). Additionally, a new characteristic peak was appeared at 1732 cm^{-1} , which was attributed to the carbonyl ($\text{C}=\text{O}$) groups of the aldehyde or ketone. From TG thermograms of SA and OSA, it can be observed that the latter exhibited lower thermal stability than that of the SA plausibly due to the mixture of ring-opened, degraded, and unmodified alginate chains. Ring-opened chains display less thermal stability due to weak hydrogen bonding among alginate chains [22]. Both SA and OSA displayed three distinct thermal decomposition stages (Fig. 2B). The first step occurred in the range of 50–210 °C, with a total mass loss of 7.3%. The second degradation step occurred from 220 to 270 °C and accounted for a total mass loss of 38.84%. The last stage of decomposition occurred beyond 270 °C. The OSA also displayed a TG thermogram identical to the SA, while showing lower thermal stability than that of the SA. The differential thermograms (DTG) curve further showed a steeper and a stronger decomposition peak of SA as compared to 1.0-OSA (Fig. S1, Supporting Information). As compared to the SA, the OSA began to decompose at low temperature and had a wide range of decomposition, presumably due to a mixture of ring-opened, oxidized, and unmodified alginate chains. Our results are in agreement with Ku et al. [22] who also reported less thermal stability of OSA than that of SA [22]. The ^1H NMR spectra further showed the formation of oxidative products (Fig. 2(C)). A new signal was observed at 1.18 ppm which was attributable to the formation of the alkyl groups due to the ring opening. Meanwhile, the splitting of the linked H-5 signal representing the guluronate-guluronate of the SA at 3.65–4.15 ppm further confirmed the opening of the ring.

The Dox (%) of OSA varied with the amount of the oxidant (Fig. 2(D)). With an increase in the content of the oxidant, the Dox (%) of the OSA was increased from 29.26% to 58.39%. The Dox (%) was found to be the highest at NaIO_4 /SA molar ratio of 1.0 and was decreased thereafter.

3.2. Properties of fibers

3.2.1. Characterization of oxidized sodium alginate based nanofibers

Electrospun membranes were prepared by using OSA with varying Dox (%) (e.g., 0.6-OSA, 0.8-OSA, 1.0-OSA, etc.) and cross-linked with the different concentrations of ADH (0.0, 0.05, 0.1, 0.5, 1.0 wt%). The representative SEM micrographs are displayed in Fig. S2 (Supporting Information). The diameter of fibers was increased with an increase in the concentration of ADH at similar Dox (%) of OSA (Fig. 3(A)).

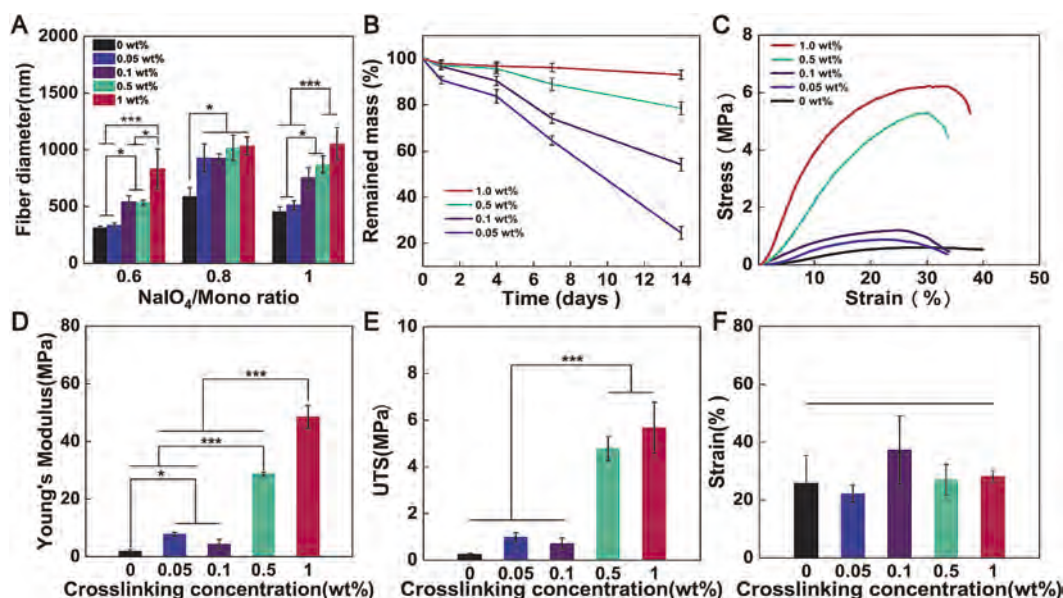


Fig. 3. Characterization of OSA fibers. (A) Average diameter of fibers prepared by using OSA with varying Dox (%) and crosslinked with the different concentrations of ADH. (B) Mass loss curves of OSA-0.8 fibers immersed in PBS for up to 14 days for *in vitro* degradation. (C–F) Mechanical properties of OSA fibers with a Dox (%) value of 48 % and crosslinked with various weight percentages of ADH. Representative stress-strain curves (C), *E* (D), UTS (E), and *E_b* (F). Fibers crosslinked with the low concentrations of ADH (0.05 and 0.1 wt%) did not significantly differ in terms of UTS, *E*, and *E_b*. In contrast, fibers crosslinked with 0.5 and 1 wt% of ADH displayed significantly higher *E* and UTS as compared to fibers crosslinked with the lower content of ADH, while there was an insignificant difference among groups in terms of *E_b*. $n = 3$ (B) and $n = 5$ (C–F). One-way analysis of variance (ANOVA) with Tukey's multiple comparison tests was used for statistical analysis. $p \leq 0.05$ was considered to be statistically significant.

Noticeably, at similar concentrations of the crosslinking agent, the diameters of fibers prepared by using OSA of varying Dox (%) were different (Fig. 3(A)). Membranes prepared by using 0.8-OSA (Dox, ~48%) and crosslinked with 0.5 wt% of ADH afforded smooth and uniform fibers. Consequently, 0.8-OSA (Dox, ~48%) and ADH (0.5 wt%) were employed for the subsequent experiments.

In vitro degradation of membranes further revealed that the fibers became morphologically stable with an increase in the concentration of the cross-linking agent. The weight of fibers crosslinked with 1 wt% ADH hardly changed over time after in PBS (Fig. 3(B)). On the other hand, when the concentration of the ADH was reduced for up to 0.05%, the fibers were almost completely dissolved by day 14 (Fig. S3, Supporting Information). In addition, by day 14, large voids were formed on the surface of the membranes due to the dissolution of fibers (Fig. S3(d), Supporting Information). These data revealed that the biodegradability of membranes can be tailored by using different concentrations of crosslinking agent. It is noteworthy to mention here that the biodegradability of membranes may also be tailored with the different Dox (%) of OSA, which however yet remains to be elucidated.

The stress-strain curves of fibers were found to be linear and obey Hooke's law (Fig. 3(C)). The *E* was increased from 4.37 MPa to 48.52 MPa (Fig. 3(D)), while the UTS was increased from 0.97 MPa to 5.67 MPa by increasing the concentrations of the crosslinking agent from 0.05 to 1 wt% (Fig. 3(E)). On the other hand, different membranes did not significantly differ in terms of strain at failure (Fig. 2(F)). By considering that the scaffolds require certain biodegradation rate as well as optimum mechanical properties, 0.5 wt% was chosen as an optimum concentration of the crosslinking agent.

3.2.2. Characterization of OSA/ZnO-NPs composite fibrous membranes

Scanning electron micrographs showed that the fibers composed of OSA/ZnO-NPs (OSA-ZnO) had a dense fibrous structure; the fibers had a smooth surface morphology without bead formation (Fig. 4(A)). The addition of ZnO-NPs did not affect the surface morphology of the fibers. The EDS images showed a homogeneous distribution of sodium and zinc elements on the fibers (Fig. 4(B–C)). The control group devoid of ZnO-

NPs did not display light spots representing the zinc element. On the other hand, other groups revealed a uniform distribution of Zn on the surface of the membranes. Moreover, the densities of light spots representing the zinc element were gradually increased with an increase in the content of ZnO-NPs.

The XRD patterns of fibers containing ZnO-NPs displayed diffraction peaks at $2\theta = 34.29^\circ$, 36.22° and 37.82° , which well-correlated with the XRD pattern of standard ZnO-NPs (Fig. 4(D)). It is noteworthy to mention here that these peaks corresponding to ZnO-NPs were only appeared in the OZ-3 membranes, which is consistent with the elemental mapping results (Fig. 4(C)). The thermal stability of the membranes containing ZnO-NPs was evaluated by TGA (Fig. 4(E)). The addition of ZnO-NPs had no obvious effect on the thermal stability of the OSA-ZnO membranes, which exhibited thermograms analogous to the SA and OSA manifesting three-step degradation profile. The effect of ZnO-NPs on the mechanical properties of OSA-ZnO composite fiber was ascertained by a uniaxial tensile testing machine (Fig. 4(F)). The fibers exhibited typical strain-strain curves (Fig. S4, Supporting Information). There was an insignificant difference among different groups in terms of UTS, while *E* was increased with an increase in the concentration of ZnO-NPs (Fig. S4 (A–B), Supporting Information). Moreover, strain at failure revealed a decreasing trend upon an increase in the concentration of ZnO-NPs (Fig. S4(C), Supporting Information).

3.3. Antibacterial activity of OSA-ZnO membranes

The contact method was employed to evaluate antibacterial properties of the OSA-ZnO composite fiber membranes against *E. coli* and *S. aureus* (Fig. 5). The incorporation of ZnO-NPs suppressed bacterial growth (Fig. 5(A)). The OSA-ZnO composite membranes revealed a concentration-dependent effect of ZnO-NPs on the antibacterial properties against both types of bacterial species. Once cultured along with OZ-2 fibers for up to 24 h, the number of colonies of *E. coli* and *S. aureus* on the agar plate were decreased to about 30% and 35%, respectively. The number of colonies of *E. coli* and *S. aureus* showed remarkable reduction with an increase in the ZnO content and were constricted to

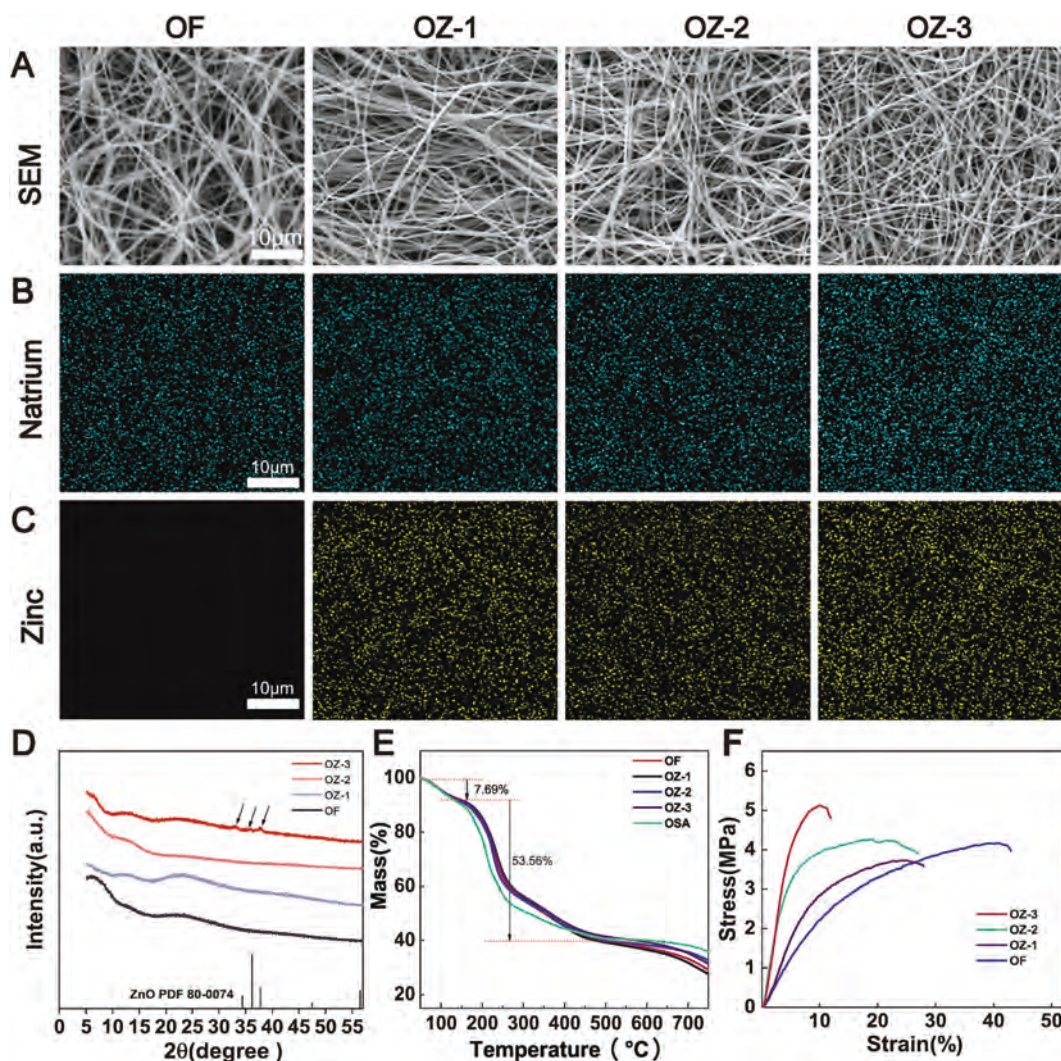


Fig. 4. Morphological and structural analysis of OSA and OSA/ZnO-NPs membranes. (A) SEM micrographs of membranes fabricated by using OSA (herein indicated by OF) and OSA/ZnO-NPs. The concentrations of ZnO-NPs were varied between 1 and 3 wt%. Sodium periodate to sodium alginate molar ratio was 0.8 (Dox, ~48%), while the concentration of the crosslinking agent was 0.5 wt%. Elemental mapping for sodium (B) and zinc (C) on membranes. XRD patterns (D), TGA thermograms (E), and representative stress-strain curves (F) of membranes. Scale bar = 10 μm (A–C). Scale bars, 10 μm (A–C). $n = 5$ (F).

4% and 10%, respectively at 3 wt% of ZnO-NPs, thereby indicating a dominant bactericidal activity of ZnO-NPs (Fig. 5(B–C)).

We also cultured both types of bacterial species on membranes and observed an interaction between the bacterial species and the fibrous membrane (Fig. 5(D)). A large number of *S. aureus* (in spherical shape) and *E. coli* (in rod shape) were observed on the OF membrane, which manifested normal morphology. However, with an increase in the content of ZnO-NPs, the number of colonies of the both types of bacterial species were gradually decreased which also corroborated results shown in Fig. 5(A). In OZ-3 group, a large number of bacterial cells were found to be dislodged; the surface was corrugated and shrunk, and decomposed into fragments, which were attached to the surface of the fiber membrane.

3.4. Cytocompatibility of OSA-ZnO membranes

Cytocompatibility of membranes was assessed by live/dead staining, SEM, and CCK-8 assay (Fig. 6). We employed NIH-3 T3 fibroblasts and HUVECs to assess the cytocompatibility of fibers. Live/dead staining at day 4 showed that the addition of ZnO-NPs had a distinct effect on cell survival (Fig. 6(A)). A large number of live cells (stained in green colour) while only a few number of dead cells (stained in red colour) were

observed on the surface of membranes (Fig. 6(A)). The OZ-3 membranes containing 3 wt% of ZnO-NPs showed markedly less cell survival than that of the OF, OZ-1 and OZ-2 membranes; less cell survival may be ascribed to the higher content of ZnO-NPs. While both types of cells exhibited typical fusiform morphology on OF membranes as well as on fibrous membranes containing low content of ZnO-NPs, they displayed circular morphology on fibrous membranes containing the high content of ZnO-NPs (Fig. 6(B)). From day 1 to day 7, NIH-3 T3 fibroblasts (Fig. 6(C)) and HUVECs (Fig. 6(D)) proliferated well on the fibrous membrane. However, the proliferation rate of both types of cells on OF membrane was significantly higher than that on the OSA-ZnO membranes. The OZ-3 membranes showed an inhibitory effect on cell proliferation. Castellano et al. [35] also observed less adhesion of fibroblasts on ionically-crosslinked alginate-based fibers, especially, for those containing ZnO-NPs than that of collagen membranes. The less growth of cells in ZnO-NPs containing membranes may be attributed to the ZnO-NPs.

It has been reported that ZnO-NPs may be cytotoxic for certain types of mammalian cells depending on the grade of the acidic environment of each cell type, which may cause dissolution of ZnO-NP, internalization of Zn^{2+} , and mitochondrial damage mediated by Zn^{2+} [40]. As can be seen from Fig. 6, cells spread nicely on OF membranes, while less on the membranes containing ZnO-NPs. While cells seeded on OZ-1 and OZ-2

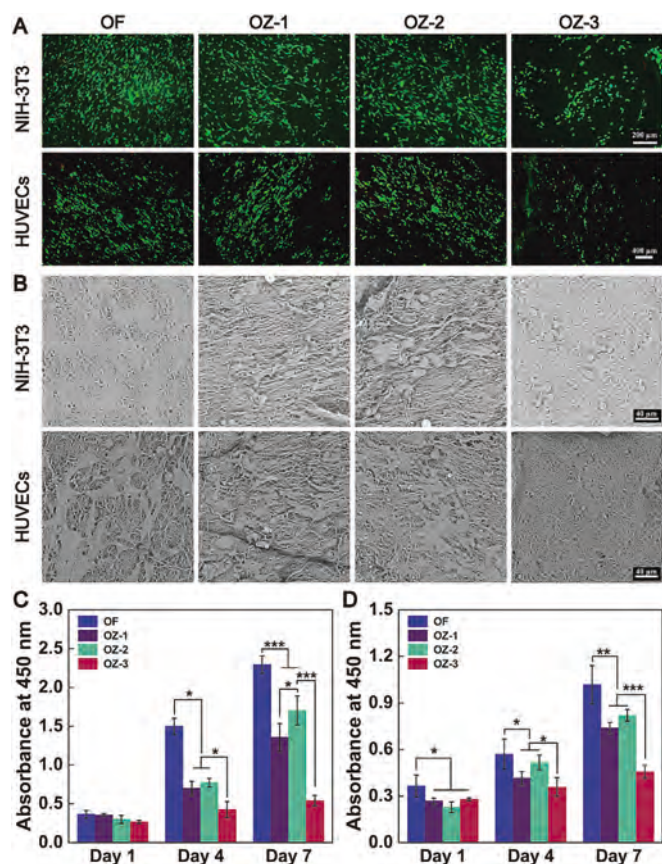


Fig. 5. *In vitro* antibacterial performance of composite fiber membranes. Macroscopic images of the colonies of *E. coli* (upper row) and *S. aureus* (lower row) grown on broth agar plates after treatment with different groups (A). Quantitative analysis of the survival rate of *E. coli* (B) and *S. aureus* (C) on membranes. SEM micrographs showing the growth of both types of bacterial species on the surface of composite fibers. Scale bar, 1-cm (A) and 8- μ m (D). ($n = 3$). One-way analysis of variance (ANOVA) with Tukey's multiple comparison tests was used for statistical analysis. $p \leq 0.05$ was considered statistically significant.

membranes showed spread morphology similar to the OF membrane, those cultured on OZ-3 membranes exhibited circular morphology, thereby indicating that the higher concentrations of ZnO-NPs may constrict cell spreading and elongation (Fig. 6(B)). Our results are in agreement with Jayakumar et al. [41] who also observed rounded cell morphology beyond 2 wt% of ZnO-NPs in sodium alginate/poly(vinyl alcohol)/ZnO composite fibers both at 48 h and 96 h [41].

3.5. *In vivo* wound healing

To evaluate wound healing effect of composite fiber membranes, a full-thickness skin incision model in rats was used. During the course of skin repair, wounds were photographed at day 3, 7, and 14 post-operatively and quantitatively analyzed for wound area to evaluate wound closure efficiency (Fig. 7(A–B)). By day 14, wounds treated with the OZ-2 membranes revealed significant healing effect. On the other hand, untreated wounds or OF-treated wounds exhibited an incomplete healing. By day 3, the OZ-2 group showed significantly less wound area ($73.8 \pm 4.6\%$) than that of the control ($98.6 \pm 6.7\%$) and OF ($96.5 \pm 5.3\%$) groups. Intriguingly, by day 14, the unhealed wound area in the OZ-2 group was reduced to only about 6.4%, while the control group still had 46.96% of the unhealed area. These results show an obvious advantage of composite fiber membranes for wound healing than that of the membranes devoid of ZnO-NPs.

H&E staining further showed an insufficient regeneration of the

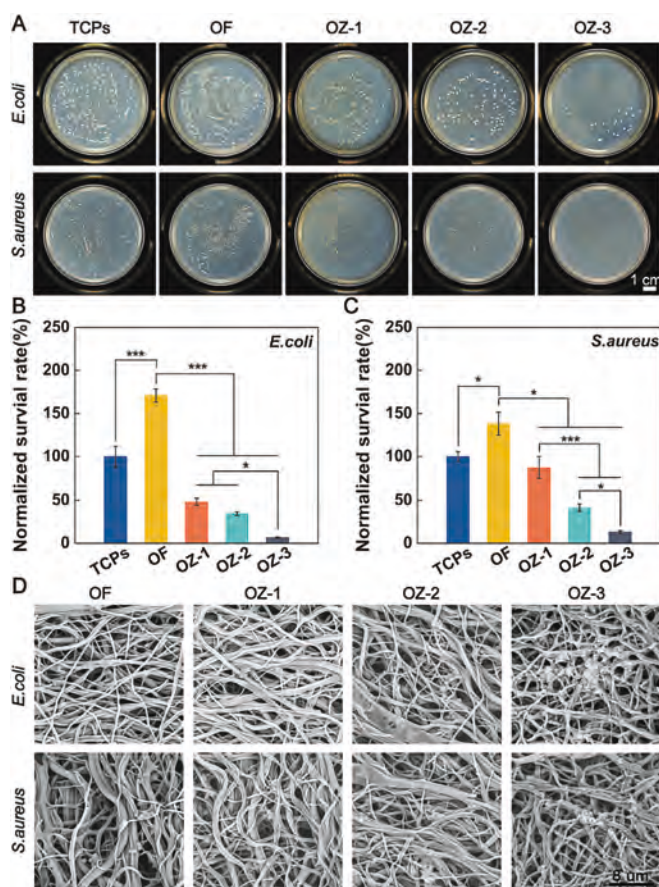


Fig. 6. Biocompatibility of different types of composite fiber membranes. (A) Live/dead assay of NIH-3T3 fibroblasts and HUVECs seeded on membranes ($n = 4$). Scale bars, upper panel, 200 μ m and lower panel 400 μ m. (B) Adhesion of both types of cells to the fiber membranes as assessed by SEM. Scale bar, 40 μ m. The CCK-8 assay of NIH-3 T3 fibroblasts (C) and HUVECs (D). Statistical analysis was performed with one-way ANOVA followed by Tukey's multiple comparison test. ($n = 4$, * $p < 0.05$).

epidermis in the control and OF groups along with an accumulation of inflammatory cells by day 3 (Fig. 7(C)). Moreover, as revealed by MT staining, wounds treated with OZ-2 fibers led to more deposition of collagen; collagen fibers were tightly-packed in the wounds treated with OZ-2 membranes as compared to the control or OF groups (Fig. 7(D)). Specifically, by day 14, the wounds treated with OZ-2 fibers exhibited complete epithelialization, showing formation of an intact stratum corneum and the basal layer as well as well-organized collagen regeneration.

To gain further insight into angiogenesis and inflammatory response, tissue sections were stained with CD31 (endothelial cell marker), CD68 (pro-inflammatory, M1-type macrophages) and CD206 (anti-inflammatory, M2-type macrophages) as well as were quantitatively analyzed (Fig. S5, Supporting Information). Animals treated with OZ-2 fibers exhibited higher angiogenesis as evidenced by the more number of capillaries and blood vessels (Fig. 8(A)). On the other hand, control and OF groups did not significantly differ in terms of the number of new capillaries (Fig. S5(A), Supporting Information). Moreover, wounds treated with OZ-2 composite fibers also showed higher expression of CD68 positive marker indicating slightly higher content of pan-macrophages than that of the control or OF groups (Fig. 8(A) and Fig. S5(B), Supporting Information). We further analyzed macrophages polarization from M1 to M2 phenotypes. Quantitative analysis revealed significantly higher number of CD206⁺ M2 macrophages than that of CD86⁺, M1 macrophages in OZ-2 treated wounds (Fig. S5(C–D),

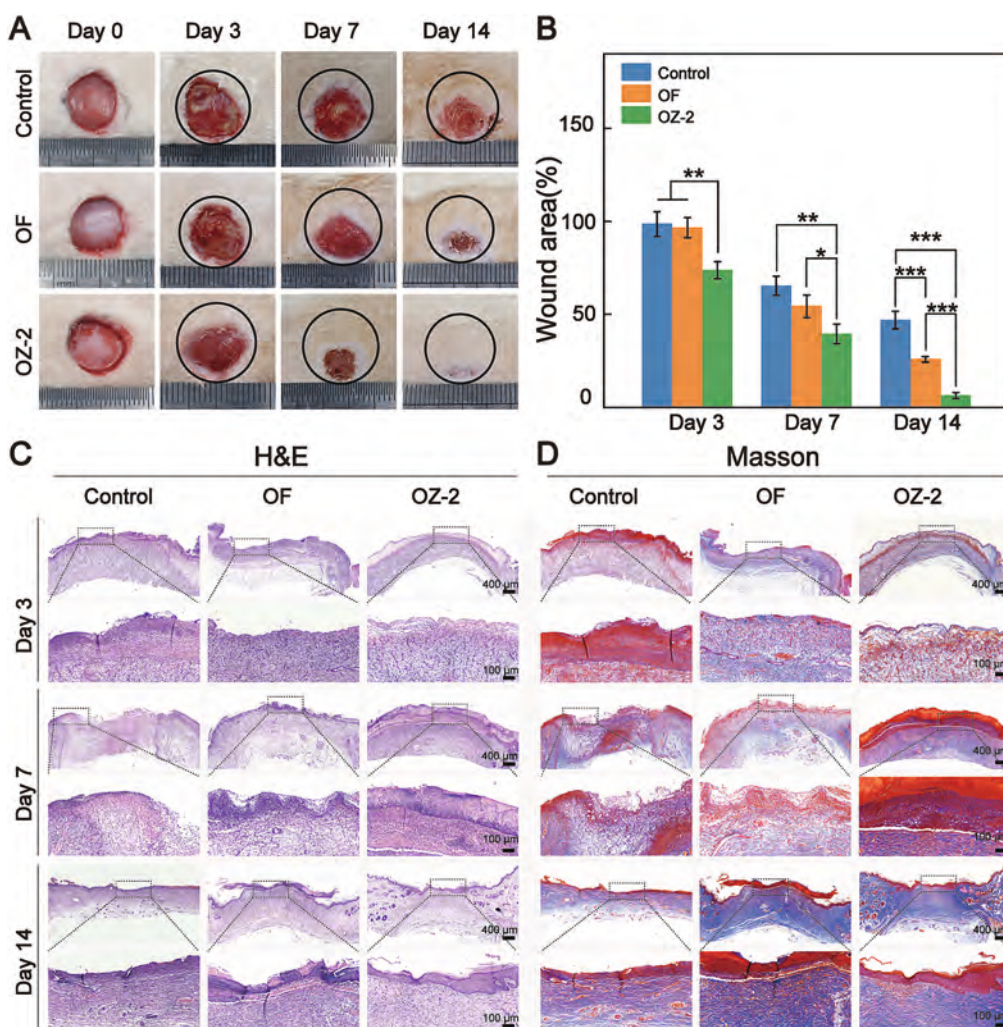


Fig. 7. Effect of composite fibers on wound healing. (A) Representative images showing wound healing at different time points for up to day 14. (B) Wound closure of various groups. (C) Histological analysis of retrieved specimens by using hematoxylin and eosin (H&E). Masson's trichrome (MT) staining of retrieved tissues at day 3, 7, and 14 post-operatively (D). ($n = 3$, $* P < 0.05$). Scale bars are shown on each photograph. Scale bar, C–D. Upper panel, 400 μm and lower panel, 100 μm at day 3, 7, and 14.

Supporting Information). In contrast, wounds which were either left untreated or were treated with OF membranes were dominated by the CD86⁺ macrophages (Fig. S5(C), Supporting Information).

4. Discussion

Wound dressings play a pivotal role for skin repair. Besides, therapeutics, growth factors, and other such bioactive cues can be incorporated into dressings to influence different stages of wound healing as well as resolve inflammatory response and exert bactericidal effect. Natural polymers, including SA exhibit good potential for biomedical applications, which have also been exploited as tissue engineered scaffolds. However, the poor spinnability of SA hampers its applicability for TE. It is worthy to note that micro/nanofibers as well as hydrogels have been developed by blending SA along with different types of natural/synthetic polymers and decellularized extracellular matrix (dECM) [41–44]. Moreover, a series of antibacterial NMs, such as silver and ZnO-NPs has been incorporated into SA-based scaffold materials to further improve their bactericidal properties [45,46]. While SA-based micro/nanofibers and hydrogels can be crosslinked with different types of bivalent ions, crosslinking through chemical conjugation based approaches may enable robust scaffold materials with chemical, mechanical, and dimensional stability. A series of natural and synthetic crosslinkers has been employed to fabricate polysaccharides and protein-based scaffolds [47].

Besides, polysaccharides, including SA can be modified to afford a

variety of functional groups to afford *in situ* crosslinking or bio-conjugation with an array of natural/synthetic polymers and bioactive cues [48–50]. The oxidation of SA may have several benefits, including the production of multiple functional aldehyde groups on the backbone of the OSA, decreased molecular weight and viscosity, and improved biodegradability, which may also be advantageous for drug delivery and TE applications [51–54]. Alginates are relatively stiff polymers and are often characterized to be semi-crystalline; the partial ring-opening of alginates may have substantial effects on chain flexibility. The flexible molecular hinges on partially-oxidized alginate may be exploited to afford a range of structures, including molecular origami. Moreover, hydrolytic lability of chains can be harnessed to tailor biomaterials with the degradability *in vitro* and *in vivo*. Consequently, we have synthesized OSA displaying varying ODs by tailoring the oxidant/SA molar ratios and optimized electrospinning parameters to afford smooth and uniform fiber morphology. Besides, we optimized concentration of the cross-linking agent (ADH) to afford water-insoluble membranes and harnessed ZnO-NPs to realize multifunctional antibacterial membranes.

It has been previously shown that OSA prepared by ethanol–water mixture was more efficient in terms of the crosslinking of different types of proteins containing amino ($-\text{NH}_2$) groups, such as collagen and gelatin [55]. We prepared OSA exhibiting different Dox (%) by finely tuning the amount of the oxidant (Fig. 1). Our ¹H NMR results were consistent with the previous report [56]. The TGA results revealed similar thermal decomposition profiles of OSA and SA (Fig. S6, Supporting Information). The first step involved the loss of bound water in

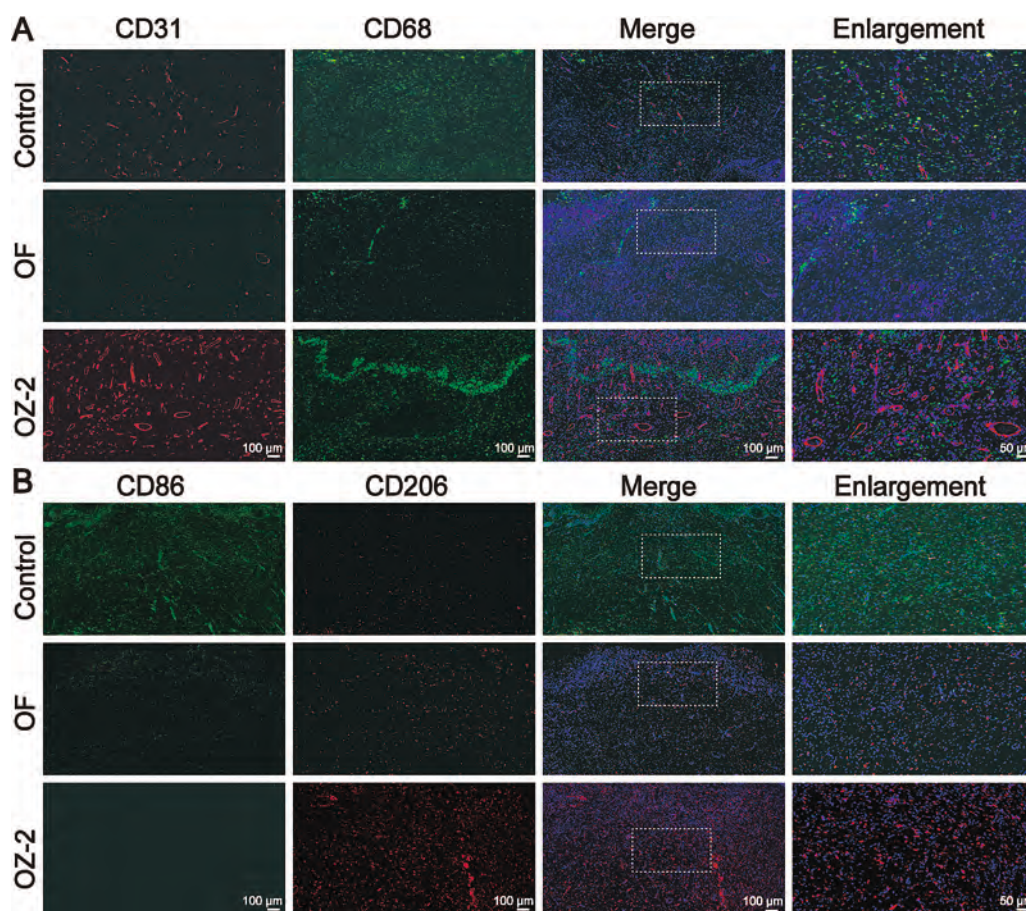


Fig. 8. Immunofluorescence staining of tissue sections for CD31-positive endothelial cells and different types of inflammatory markers, including CD68, CD86, and CD206 for angiogenesis and inflammatory response at day 7 post-operatively. The CD31⁺ cells (stained in red in A), CD68⁺ pan-macrophages (stained in green in A), CD86⁺ M1 macrophages (stained in green in B), and CD206⁺ M2 macrophages (stained in red in B). Scale bars. A–B: first three panels, 100 μm and the right most panel, 50 μm.

the SA. During the second step, the SA was degraded, and the hydroxyl (—OH) groups on the adjacent molecular chains were removed in the form of water molecules. The last degradation step involved the oxidation and decomposition of the SA to yield sodium oxide (Na₂O) [22,57]. Besides, DTG curves, revealed a steeper and a stronger decomposition peak of SA than that of the OSA (Fig. S1, Supporting Information). The thermograms of OSA and OSA/ZnO-NPs also resembled the SA (Fig. 2 (B), Fig. 4(E), and Fig. S1, Supporting Information). The uneven base line in the thermograms may be ascribed to an earlier degradation and lower thermal stability of OSA (Fig. S6, Supporting Information). Since OSA is a mixture of ring-opened, degraded, and unmodified alginate chains, it may show less thermal stability as well as a wide range of decomposition. Our results are in agreement with Ku et al. [22] and Hajiabbas et al. [57] who also observed lower thermal stability of OSA as well as an earlier degradation and broad range of decomposition as compared to the SA. The excessive amount of the NaIO₄ may further oxidize the aldehyde groups to the carboxylic (—COOH) groups or hemiacetals [58], thereby resulting into a reduction in the content of the aldehyde groups, which is also reflected from our results that the Dox (%) was reduced after attaining a maxima.

The ADH is a bifunctional cross-linking agent, which can react with the active aldehyde groups on the molecular chain of OSA to form stable hydrazone bonds and may prevent water solubility of the membranes [59]. We found a significant effect of the different concentrations of crosslinking agent on the fiber diameter and physico-chemical properties of the OSA fibers (Fig. S2, Supporting Information). The 0.8-OSA (Dox, ~48%) was optimized based on the fiber diameter and was further screened for an appropriate concentration of the crosslinking agent. The degradation performance and mechanical properties of the fibers can be adjusted according to the ADH content. Finally, 0.5 wt% of ADH was found to be an optimum concentration of the crosslinking

agent, which afforded uniform fiber diameter, good degradation performance, and sufficient mechanical properties. While ZnO-NPs did not influence the surface morphology and thermal stability of the OSA-ZnO hybrids (Fig. 4), they were found to improve the *E* while decrease the *E_b* of membranes [60]. Mo et al. [27] observed an increase in the UTS while a decrease in *E_b* in PLGA/silk fibroin based fibers with the addition of ZnO-NPs. Nonetheless, composite OSA/ZnO-NPs based membranes exhibited sufficient mechanical properties as required for wound dressings [26].

ZnO-NPs are widely exploited as antibacterial agents [61,62]. The improved antibacterial activity of membranes is attributable to the release of Zn²⁺, which may not only electrostatically interact with the negatively-charged bacterial membranes but may also increase the permeability of bacterial cell membranes, thereby triggering bacterial cell death [63]. Besides, ZnO-NPs can exert bactericidal effects via the decomposition of the outer membranes of bacterial species by ROS and hydroxyl radicals (OH[•]), which may lead to the peroxidation of phospholipid as well as the apoptosis of bacterial species. It has also been previously reported that ZnO-NPs can be physically adhered to a bacterial cell wall to induce cell apoptosis [64,65]. However, suitable carriers are required to fully harness the potential of ZnO-NPs for inducing antibacterial action at the wound site. The OSA-ZnO membranes showed dominant antibacterial effects against both types of bacterial species, including *E. coli* and *S. aureus* by remarkably suppressing the number of bacterial colonies as well as inducing bacterial rupture and deformation from the surface of membranes (Fig. 5) [66]. Our results are in agreement with Wu et al. [26] and Khan et al. [27] who also observed significant antibacterial effect of ZnO-NPs against *E. coli* and *S. aureus* in poly(L-lactide-co-glycolide)/gelatin (PLGA/Gel) and PLGA/silk fibroin based membranes. Similarly, Zia et al. [67] and Jamil et al. [68] observed significant antibacterial effect of ZnO-NPs against different

types of bacterial species. While exact mechanism about ZnO-NPs mediated antibacterial effect yet remains to be explored, the structural deformation of bacterial species directly cultured on membranes may plausibly be ascribed to an electrostatic interaction between bacterial cell wall and ZnO-NPs.

Once assessed for the cytocompatibility, we found that the membranes containing the high content of ZnO-NPs hindered cell proliferation, which can be ascribed to an overproduction of ROS, thereby impeding cell proliferation (Fig. 6) [69]. On the other hand, membranes containing low concentrations of ZnO-NPs may improve cell proliferation [27]. Beside influencing cell proliferation, ROS may also impact the biocompatibility of biomaterials. The higher oxidative stress is often associated with inflammation. Pro-inflammatory response may lead to an overproduction of inflammatory cytokines, including tumor necrosis factor alpha (TNF- α), interleukin-6 (IL-6), and interleukin-1 beta (IL-1 β), thereby further impairing the healing response. On the other hand, anti-inflammatory cytokines, such as IL-4 and IL-10 have been associated with the inflammation resolution and improved healing. Accordingly, numerous strategies have been put forwarded to reduce the oxidative stress, which were found to resolve inflammation, afford anti-oxidative environment, and improve biocompatibility [70–73]. Consequently, owing to their good cytocompatibility and antibacterial properties, OZ-2 membranes containing 2 wt% of ZnO-NPs were chosen for the subsequent *in vivo* studies.

It is noteworthy to mention here that we leveraged electrospun membranes for wound healing owing to their ECM-mimetic morphology and their ability to support the diffusion and transport of oxygen and nutrients, while simultaneously maintaining the moisture of the wound [74–76]. Altogether, these ECM-mimetic membranes may have a positive effect on wound repair [77]. Indeed our *in vivo* results displayed good wound healing effect of OZ-2 membranes than that of the untreated wounds or those treated with the OF membranes (Fig. 7(A)). H&E staining of the OZ-2-treated group showed complete epithelialization along with the formation of an intact stratum corneum and basal layer (Fig. 7(B)), which was consistent with the macroscopic findings of the wounds for up to different time points (Fig. 7(A)). Collagen, being the main component of the ECM can prevent matrix degradation as well induce formation of granulation tissues and capillaries, thereby playing a pivotal role for tissue repair [78]. Consequently, OZ-2 membranes significantly promoted the deposition of collagen during wound healing (Fig. 7(C)). By day 7, the wound surface treated with OZ-2 membrane had the highest amount of collagen production, which became further evident by day 7, thereby replicating the morphology features of normal tissue.

The wound injury is often accompanied by the damage or even the loss of vascular tissues in the dermis. Since vascular networks can provide oxygen and nutrients for the proliferation, growth, and migration of various cell types as well as improve the transport of nutrients and metabolites, the induction of vascular network holds great promise for wound healing [79]. As ZnO-NPs can produce ROS, including superoxide (O₂⁻) and hydrogen peroxide (H₂O₂), they can promote angiogenesis and cell proliferation by stimulating the production of a series of growth factors, such as vascular endothelial growth factor (VEGF) and fibroblast growth factor (FGF) [61,80]. By the day 7, wounds treated with OZ-2 membranes showed significant regeneration of blood vessels as compared to the control and OF membranes (Fig. 8(A)).

Inflammatory microenvironment may either promote or delay tissue repair. A variety of inflammatory cell types, including macrophages and T cells participate in wound healing. Macrophages have been shown to display different phenotypes, including pro-inflammatory (M1) and anti-inflammatory (M2); the latter types of cells have been shown to be the key mediators of inflammation resolution and tissue repair. Therefore, explants from wounds were evaluated for different types of inflammatory cells, with the aim to elucidate their effect on tissue repair. The CD68⁺ is a pan-macrophages marker that is activated during the early stages of inflammation. It may recognize and phagocytize necrotic

tissues, cellular debris and pathogens, thereby inhibiting the development of inflammation in the wound [81]. The CD68⁺ macrophages can also promote bioactive factors, such as platelet-derived growth factor-beta (PDGF- β) as well as enzymes, including collagenase and elastase [82], which may play an important role to promote the formation of granulation tissues and accelerate wound healing. The ZnO-NPs can regulate the number of macrophages, modulate inflammatory response, and promote epithelialization [20]. Due to their high plasticity, macrophages can respond to various local environmental signals and may either polarize toward pro-inflammatory phenotypes (M1, CD86⁺) or anti-inflammatory phenotypes (M2, CD206⁺) (Fig. 8(A–B)) [83–85]. We found significantly higher number of CD68⁺ and CD206⁺ macrophages, while remarkably less number of CD86⁺ macrophages in wounds treated with OZ-2 composite fibers than that of the other groups. These results reveal that OZ-2 membranes can promote the polarization of macrophages toward an anti-inflammatory phenotype, which may accelerate wound repair through the secretion of anti-inflammatory factors [86]. Nonetheless, it necessitates mechanistic insight to further elucidate the beneficial effect of anti-inflammatory macrophages on improved wound healing.

This study has also certain limitations. First, we employed only a limited number of cell types for the evaluation of biocompatibility of membranes, including fibroblasts and HUVECs. Since wound healing involves an array of cell types, including keratinocytes, epithelial cells, fibroblasts, endothelial cells, and inflammatory cell types, detailed biocompatibility assessment of membranes is warranted in future studies [87,88]. Besides, in the cytocompatibility assay of composite fiber membranes, we did not employ negative or positive control groups, which may provide an additional insight for *in vitro* and *in vivo* applications of scaffolds. Second, while we discerned the biocompatibility of fibrous OSA/ZnO-NPs membranes, the comparison with fibrous SA/ZnO-NPs may have further helped clearly articulate the biocompatibility of wound dressings. Besides, we did not include positive or negative groups in the cytocompatibility assay, which may have also clearly helped articulate the biocompatibility of composite fibrous membranes. It is noteworthy to mention here that Castellano et al. [35] designed ZnO-NPs containing ionically-crosslinked SA-based membranes, which displayed good cytocompatibility for fibroblasts and keratinocytes. Third, while we have assessed an antibacterial effect of OZ membranes against different types of bacterial species, including *E. coli* and *S. aureus*, a detailed mechanistic understanding yet remains to be evaluated. Fourth, we have employed simple wound healing model without diabetes and infection, the evaluation of these membranes in these models may further help evaluate their reparative potential. Nonetheless, we have demonstrated the successful preparation of OSA as well as its electrospinning and chemical crosslinking to afford water insoluble nanofibrous membranes. Besides, we observed significant antibacterial effect and superior wound healing in composite nanofibrous membranes containing ZnO-NPs.

5. Conclusions

Conclusively, we synthesized OSA with varying oxidation degrees to improve its spinnability and blended it along with ZnO-NPs to fabricate electrospun bandages for wound healing. We systematically optimized the conditions to precisely control the oxidation of SA as well as determined the optimal conditions for the crosslinking of OSA/ZnO-NPs membranes by using ADH. Consequently, 0.8-OSA membranes (Dox, ~48 %) and 0.5 wt% ADH were shown to afford membranes with good morphology, mechanical properties, and biocompatibility. Similarly, while we employed different concentrations of ZnO-NPs for up to 3 wt%, we found that the membranes containing 2 wt% of ZnO-NPs were suitable in terms of biocompatibility *in vitro*, which further displayed good antibacterial properties against different bacterial species, including *E. coli* and *S. aureus in vitro*. Membranes containing 2 wt% of ZnO-NPs (OZ-2) also displayed remarkably higher epithelialization, collagen

deposition, and vascularization as compared to untreated wounds (negative control) and OF membranes (control group) in a full-thickness excisional wound defect model in rats. In addition, OSA-ZnO composite fibers attenuated the inflammatory response, induced macrophage polarization toward M2 phenotypes, and promoted the granulation tissue formation. Taken together, these data show that nanofibrous membranes consisting of OSA/ZnO-NPs could be good candidates for the fabrication of electrospun membranes for wound healing, which are also worthy of investigations for other bio-related disciplines.

CRedit authorship contribution statement

Wei Wang & Mingyue Liu: Investigation, Methodology, Experimental data acquisition, Writing - Original draft.

HaiYan Li & Rashida Hashim: Investigation, Methodology, Experimental data acquisition.

Mohamed EL-Newehy, Hany EL-Hamshary, and Yosry Morsi: Validation, Visualization, Funding Acquisition.

Muhammad Shafiq: Investigation, Funding Acquisition, Visualization, Writing - Review & Editing.

Xiumei Mo: Funding acquisition, Supervision, Writing - Original draft, Writing Review & Editing.

Declaration of competing interest

The authors declare the following financial interests/personal relationships which may be considered as potential competing interests: Xiumei Mo reports was provided by Donghua University, Shanghai, China.

Data availability

Data will be made available on request.

Acknowledgments

This research received partial support from National Natural Science Foundation of China (Project # 32050410286), Science and Technology Commission of Shanghai Municipality (No. 19441902600, 20S31900900, 20DZ2254900) and Sino German Science Foundation Research Exchange Center (M-0263). This project was also supported by Researchers Supporting Program of King Saud University, Riyadh, Saudi Arabia (RSP2023R65), and National Advanced Functional Fiber Innovation Center (2021-fx020301). This research was also partly supported by the Grant-in-Aid for JSPS Fellows (Project # JP21F21353). M.S is an International Research Fellow of the Japan Society for the Promotion of Science (Postdoctoral Fellowships for Research in Japan (Standard)).

Appendix A. Supplementary data

Supplementary data to this article can be found online at <https://doi.org/10.1016/j.ijbiomac.2023.123480>.

References

- T. Velnar, T. Bailey, V. Smrkoli, The wound healing process: an overview of the cellular and molecular mechanisms, *J. Int. Med. Res.* 37 (2009) 1528–1542, <https://doi.org/10.1177/147323000903700531>.
- M. Plummer, C. de Martel, J. Vignat, J. Ferlay, F. Bray, S. Franceschi, Global burden of cancers attributable to infections in 2012: a synthetic analysis, *Lancet Glob. Health* 4 (9) (2016) e609–e616, [https://doi.org/10.1016/S2214-109X\(16\)30143-7](https://doi.org/10.1016/S2214-109X(16)30143-7).
- M. Shafiq, T. Yasin, M.A. Rafiq, Shaista, Structural, thermal, and antibacterial properties of chitosan/ZnO composites, *Polym. Compos.* 35 (2014) 79–85, <https://doi.org/10.1002/pc.22636>.
- A. Khan, S. Mehmood, M. Shafiq, T. Yasin, Z. Akhter, S. Ahmad, Structural and antimicrobial properties of irradiated chitosan and its complexes with zinc, *Radiat. Phys. Chem.* 91 (2013) 138–142, <https://doi.org/10.1016/j.radphyschem.2013.05.025>.
- Z. Zhou, D. Yan, X. Cheng, M. Kong, Y. Liu, C. Feng, X. Chen, Biomaterials based on N, N, N-trimethyl chitosan fibers in wound dressing applications, *Int. J. Biol. Macromol.* 89 (2016) 471–476, <https://doi.org/10.1016/j.ijbiomac.2016.02.036>.
- P. Zarrintaj, A.S. Moghaddam, S. Manouchehri, Z. Atoufi, A. Amiri, M. A. Amirkhani, M.A. Nilforoushzadeh, M.R. Saeb, M.R. Hamblin, M. Mozafari, Can regenerative medicine and nanotechnology combine to heal wounds? The search for the ideal wound dressing, *Nanomedicine* 12 (2017) 2403–2422, <https://doi.org/10.2217/nmm-2017-0173>.
- M. Shafiq, O. Ali, S. Han, D. Kim, Mechanobiological strategies to enhance stem cell functionality for regenerative medicine and tissue engineering, *Front. Cell. Dev. Biol.* 9 (2021), 747398, <https://doi.org/10.3389/fcell.2021.747398>.
- A. Greiner, J.H. Wendorff, Electrospinning: a fascinating method for the preparation of ultrathin fibres, *Angew. Chem. Int. Ed.* 46 (2007) 5670–5703, <https://doi.org/10.1002/anie.200604646>.
- R.G. Flemming, C.J. Murphy, G.A. Abrams, S.L. Goodman, P.F. Nealey, Effects of synthetic micro- and nano-structured surfaces on cell behavior, *Biomaterials* 20 (1999) 573–588, [https://doi.org/10.1016/S0142-9612\(98\)00209-9](https://doi.org/10.1016/S0142-9612(98)00209-9).
- Y. Chen, X. Dong, M. Shafiq, G. Myles, N. Radacsi, X. Mo, Recent advancements on three-dimensional electrospun nanofiber scaffolds for tissue engineering, *Adv. Fiber. Mater.* 4 (2022) 959–986, <https://doi.org/10.1007/s42765-022-00170-7>.
- Y. Chen, M. Shafiq, M. Liu, Y. Morsi, X. Mo, Advanced fabrication for electrospun three-dimensional nanofiber aerogels and scaffolds, *Bioact. Mater.* 5 (2020) 963–979, <https://doi.org/10.1016/j.bioactmat.2020.06.023>.
- K. Ye, H. Kuang, Z. You, Y. Morsi, X. Mo, Electrospun nanofibers for tissue engineering with drug loading and release, *Pharmaceutics* 11 (2019) 182, <https://doi.org/10.3390/pharmaceutics11040182>.
- E. Venugopal, N. Rajeswaran, K.S. Sahanand, A. Bhattacharyya, S. Rajendran, In vitro evaluation of phytochemical loaded electrospun gelatin nanofibers for application in bone and cartilage tissue engineering, *Biomed. Mater.* 14 (2018), 015004, <https://doi.org/10.1088/1748-605X/aae3ef>.
- A. Sadeghi, F. Moztaarzadeh, J.A. Mohandesi, Investigating the effect of chitosan on hydrophilicity and bioactivity of conductive electrospun composite scaffold for neural tissue engineering, *Int. J. Biol. Macromol.* 121 (2019) 625–632, <https://doi.org/10.1016/j.ijbiomac.2018.10.022>.
- Q. Sun, J. Si, L. Zhao, T. Wei, T. Wang, F. Li, Y. Li, M. Shafiq, L. Wang, R. Liu, D. Zhi, K. Wang, Direct thrombin inhibitor-bivalirudin improved the hemocompatibility of electrospun polycaprolactone vascular grafts, *Compos. Part B. Eng.* 234 (2022), 109702, <https://doi.org/10.1016/j.compositesb.2022.109702>.
- X. Dou, Q. Wang, Z. Li, J. Ju, S. Wang, L. Hao, K. Sui, Y. Xia, Y. Tan, Seaweed-derived electrospun nanofibrous membranes for ultrahigh protein adsorption, *Adv. Funct. Mater.* 29 (2019), 1905610, <https://doi.org/10.1002/adfm.201905610>.
- M.A. Taemeh, A. Shiravandi, M.A. Korayem, H. Daemi, Fabrication challenges and trends in biomedical applications of alginate electrospun nanofibers, *Carbohydr. Polym.* 228 (2020), 115419, <https://doi.org/10.1016/j.carbpol.2019.115419>.
- F. Sun, J. Guo, Y. Liu, Y. Yu, Preparation, characterizations and properties of sodium alginate grafted acrylonitrile/polyethylene glycol electrospun nanofibers, *Int. J. Biol. Macromol.* 137 (2019) 420–425, <https://doi.org/10.1016/j.ijbiomac.2019.06.185>.
- Q. Wang, J. Ju, Y. Tan, L. Hao, Y. Ma, Y. Wu, H. Zhang, Y. Xia, K. Sui, Controlled synthesis of sodium alginate electrospun nanofiber membranes for multi-occasion adsorption and separation of methylene blue, *Carbohydr. Polym.* 205 (2019) 125–134, <https://doi.org/10.1016/j.carbpol.2018.10.023>.
- S.I. Jeong, M.D. Krebs, C.A. Bonino, S.A. Khan, E. Alsborg, Electrospun alginate nanofibers with controlled cell adhesion for tissue engineering, *Macromol. Biosci.* 10 (2010) 934–943, <https://doi.org/10.1002/mabi.201000046>.
- H. Nie, A. He, J. Zheng, S. Xu, J. Li, C.C. Han, Effects of chain conformation and entanglement on the electrospinning of pure alginate, *Biomacromolecules* 9 (2008) 1362–1365, <https://doi.org/10.1021/bm701349j>.
- M.K. Ku, Y. Ahn, Y. Song, Y.-H. Yang, H. Kim, Effect of oxidized alginate on its electrospinnability, *Fibers Polym.* 15 (2014) 1835–1841, <https://doi.org/10.1007/s12221-014-1835-y>.
- R. Aston, M. Wimalaratne, A. Brock, G. Lawrie, L. Grondahl, Interactions between chitosan and alginate dialdehyde biopolymers and their layer-by-layer assemblies, *Biomacromolecules* 16 (2015) 1807–1817, <https://doi.org/10.1021/acs.biomac.5b00383>.
- S. Wang, J. Ju, S. Wu, M. Lin, K. Sui, Y. Xia, Y. Tan, Electrospinning of biocompatible alginate-based nanofiber membranes via tailoring chain flexibility, *Carbohydr. Polym.* 230 (2020) 115–121, <https://doi.org/10.1016/j.carbpol.2019.115665>.
- M. Liu, X. Wang, H. Li, C. Xia, Z. Liu, J. Liu, A. Yin, X. Lou, H. Wang, X. Mo, J. Wu, Magnesium oxide-incorporated electrospun membranes inhibit bacterial infections and promote the healing process of infected wounds, *J. Mater. Chem. B* 9 (2021) 3727–3744, <https://doi.org/10.1039/D1TB00217A>.
- F. Wu, Z. Yuan, M. Shafiq, L. Zhang, M. Rafique, F. Yu, M. El-Newehy, H. El-Hamshary, Y. Morsi, Y. Xu, X. Mo, Synergistic effect of glucagon-like peptide-1 analogue liraglutide and ZnO on the antibacterial, hemostatic, and wound healing properties of nanofibrous dressings, *J. Biosci. Bioeng.* 134 (2022) 248–258, <https://doi.org/10.1016/j.jbiosc.2022.06.004>.
- A.U.R. Khan, K. Huang, Z. Jinzhong, T. Zhu, Y. Morsi, A. Aldabahi, M. El-Newehy, X. Yan, X. Mo, Exploration of the antibacterial and wound healing potential of a PLGA/silk fibroin based electrospun membrane loaded with zinc oxide nanoparticles, *J. Mater. Chem. B* 9 (2021) 1452–1465, <https://doi.org/10.1039/D0TB02822C>.
- N.M. Franklin, N.J. Rogers, S.C. Apte, G.E. Batley, G.E. Gadd, P.S. Casey, Comparative toxicity of nanoparticulate ZnO, bulk ZnO, and ZnCl₂ to a freshwater

- microalga (*Pseudokirchneriella subcapitata*): the importance of particle solubility, *Env. Sci. Technol.* 41 (2007) 8484–8490, <https://doi.org/10.1021/es071445r>.
- [29] H. Yang, C. Liu, D. Yang, H. Zhang, Z. Xi, Comparative study of cytotoxicity, oxidative stress and genotoxicity induced by four typical nanomaterials: the role of particle size, shape and composition, *J. Appl. Toxicol.* 29 (2009) 69–78, <https://doi.org/10.1002/jat.1385>.
- [30] A. Nel, T. Xia, L. Madler, N. Li, Toxic potential of materials at the nano level, *Science* 311 (2006) 622–627, <https://doi.org/10.1126/science.1114397>.
- [31] K.Y. Lee, D.J. Mooney, Alginate: properties and biomedical applications, *Prog. Polym. Sci.* 37 (2012) 106–126, <https://doi.org/10.1016/j.progpolymsci.2011.06.003>.
- [32] A. Doderer, L. Pianella, S. Vicini, M. Alloisio, M. Ottonelli, M. Castellano, Alginate-based hydrogels prepared via ionic gelation: an experimental design approach to predict the crosslinking degree, *Eur. Polym. J.* 118 (2019) 586–594, <https://doi.org/10.1016/j.eurpolymj.2019.06.028>.
- [33] H. Zhao, N.D. Heindel, Determination of degree of substitution of formyl groups in polyaldehyde dextran by the hydroxylamine hydrochloride method, *Pharm. Res.* 8 (1991) 400–402, <https://doi.org/10.1023/A:1015866104055>.
- [34] X. Mo, H. Iwata, S. Matsuda, Y. Ikada, Soft tissue adhesive composed of modified gelatin and polysaccharides, *J. Biomater. Sci. Polym. Ed.* 11 (2000) 341–351, <https://doi.org/10.1163/156856200743742>.
- [35] A. Doderer, S. Scarfi, M. Pozzolini, S. Vicini, M. Alloisio, M. Castellano, Alginate-based electrospun membranes containing ZnO nanoparticles as potential wound healing patches: biological, mechanical, and physicochemical characterization, *ACS Appl. Mater. Interfaces* 12 (2020) 3371–3381, <https://doi.org/10.1021/acsami.9b17597>.
- [36] T. Braschler, S. Wu, F. Wildhaber, S. Bencherif, D. Mooney, Soft nanofluidics governing minority ion exclusion in charged hydrogels, *Soft Matter* 11 (20) (2015) 4081–4090.
- [37] M. Shafiq, Y. Jung, S.H. Kim, In situ vascular regeneration using substance P-immobilized poly(l-lactide-co-ε-caprolactone) scaffolds: stem cell recruitment, angiogenesis, and tissue regeneration, *Eur. Cell. Mater* 30 (2015) 282–302, <https://doi.org/10.22203/eCM.v030a20>.
- [38] M. Shafiq, Y. Jung, S.H. Kim, Stem cell recruitment, angiogenesis, and tissue regeneration in substance P-conjugated poly(l-lactide-co-ε-caprolactone) nonwoven meshes, *J. Biomed. Mater. Res. Part A* 103 (2015) 2673–2688, <https://doi.org/10.1002/jbm.a.35400>.
- [39] M. Shafiq, Y. Zhang, D. Zhu, Z. Zhao, D.-H. Kim, S.H. Kim, D. Kong, In situ cardiac regeneration by using neuropeptide substance P and IGF-1C peptide eluting heart patches, *Regen. Biomater.* 5 (2018) 303–316, <https://doi.org/10.1093/rb/rby021>.
- [40] R. Vandebriel, W.D. Jong, A review of mammalian toxicity of ZnO nanoparticles, *Nanotechnol. Sci. Appl.* 5 (2012) 61–71, <https://doi.org/10.2147/NSA.S23932>.
- [41] K. Shalumon, K. Anulekha, S. Nair, S. Nair, K. Chennazhi, R. Jayakumar, Sodium alginate/poly(vinyl alcohol)/nano ZnO composite nanofibers for antibacterial wound dressings, *Int. J. Biol. Macromol.* 49 (2011) 247–254, <https://doi.org/10.1016/j.ijbiomac.2011.04.005>.
- [42] T. Liu, Z. Feng, Z. Li, Z. Lin, L. Chen, B. Li, Z. Chen, Z. Wu, J. Zeng, J. Zhang, J. Hong, H. Xia, L. Li, X. Ye, Y. Zhang, Carboxymethyl chitosan/sodium alginate hydrogels with polydopamine coatings as promising dressings for eliminating biofilm and multidrug-resistant bacteria induced wound healing, *Int. J. Biol. Macromol.* 225 (2023) 923–937, <https://doi.org/10.1016/j.ijbiomac.2022.11.156>.
- [43] Z. Wang, C. Liu, B. Chen, Y. Luo, Magnetically-driven drug and cell on demand release system using 3D printed alginate based hollow fiber scaffolds, *Int. J. Biol. Macromol.* 168 (2021) 38–45, <https://doi.org/10.1016/j.ijbiomac.2020.12.023>.
- [44] T. Chu, G. Tripathi, M. Park, S. Bae, B. Lee, In-vitro and in-vivo biocompatibility of dECM-alginate as a promising candidate in cell delivery for kidney regeneration, *Int. J. Biol. Macromol.* 211 (2022) 616–625, <https://doi.org/10.1016/j.ijbiomac.2022.05.085>.
- [45] M. Zhou, F. Lin, W. Li, L. Shi, Y. Li, G. Shan, Development of nanosilver doped carboxymethyl chitosan-polyamideamine alginate composite dressing for wound treatment, *Int. J. Biol. Macromol.* 166 (2021) 1335–1351, <https://doi.org/10.1016/j.ijbiomac.2020.11.014>.
- [46] M. Alloisio, A. Doderer, S. Alberti, S. Vicini, M. Castellano, Electrospun alginate mats embedding silver nanoparticles with bioactive properties, *Int. J. Biol. Macromol.* 213 (2022) 427–434, <https://doi.org/10.1016/j.ijbiomac.2022.05.183>.
- [47] A. Alavarse, E. Frachini, R. da Silva, V. Lima, A. Shavandi, D. Petri, Crosslinkers for polysaccharides and proteins: synthesis conditions, mechanisms, and crosslinking efficiency, a review, *Int. J. Biol. Macromol.* 202 (2022) 558–596, <https://doi.org/10.1016/j.ijbiomac.2022.01.029>.
- [48] L. Yuan, Y. Wu, Q. Gu, H. El-Hamshary, M. El-Newehy, X. Mo, Injectable photo-crosslinked enhanced double-network hydrogels from modified sodium alginate and gelatin, *Int. J. Biol. Macromol.* 96 (2017) 569–577, <https://doi.org/10.1016/j.ijbiomac.2016.12.058>.
- [49] V. Ravichandran, A. Jayakrishnan, Synthesis and evaluation of anti-fungal activities of sodium alginate-amphotericin B conjugates, *Int. J. Biol. Macromol.* 108 (2018) 1101–1109, <https://doi.org/10.1016/j.ijbiomac.2017.11.030>.
- [50] J. Ma, P. Wang, C. Tang, H. Liao, W. Zhang, R. Yang, T. Shi, X. Tan, B. Chi, Injectable shear-thinning sodium alginate hydrogels with sustained submucosal lift for endoscopic submucosal dissection, *Int. J. Biol. Macromol.* 223 (2022) 939–949, <https://doi.org/10.1016/j.ijbiomac.2022.11.103>.
- [51] Y. He, Y. Tian, W. Zhang, X. Wang, X. Yang, B. Li, L. Ge, D. Bai, D. Li, Fabrication of oxidized sodium alginate-collagen heterogeneous bilayer barrier membrane with osteogenesis-promoting ability, *Int. J. Biol. Macromol.* 202 (2022) 55–67, <https://doi.org/10.1016/j.ijbiomac.2021.12.155>.
- [52] K.A. Kristiansen, A. Potthast, B.E. Christensen, Periodate oxidation of polysaccharides for modification of chemical and physical properties, *Carbohydr. Polym.* 345 (2010) 1264–1271, <https://doi.org/10.1016/j.carres.2010.02.011>.
- [53] W. Ding, J. Zhou, Y. Zeng, Y. Wang, B. Shi, Preparation of oxidized sodium alginate with different molecular weights and its application for crosslinking collagen fiber, *Carbohydr. Polym.* 157 (2017) 1650–1656, <https://doi.org/10.1016/j.carbpol.2016.11.045>.
- [54] Y. Hu, L. Liu, Z. Gu, W. Dan, N. Dan, X. Yu, Modification of collagen with a natural derived cross-linker, alginate dialdehyde, *Carbohydr. Polym.* 102 (2014) 324–332, <https://doi.org/10.1016/j.carbpol.2013.11.050>.
- [55] B. Balakrishnan, S. Lesieur, D. Labarre, A. Jayakrishnan, Periodate oxidation of sodium alginate in water and in ethanol-water mixture: a comparative study, *Carbohydr. Res.* 340 (2005) 1425–1429, <https://doi.org/10.1016/j.carres.2005.02.028>.
- [56] C.G. Gomez, M. Rinaudo, M.A. Villar, Oxidation of sodium alginate and characterization of the oxidized derivatives, *Carbohydr. Polym.* 67 (2007) 296–304, <https://doi.org/10.1016/j.carbpol.2006.05.025>.
- [57] M. Hajiabbas, I. Alemzadeh, M. Vossoughi, A porous hydrogel-electrospun composite scaffold made of oxidized alginate/gelatin/silk fibroin for tissue engineering application, *Carbohydr. Polym.* 245 (2020), 116465, <https://doi.org/10.1016/j.carbpol.2020.116465>.
- [58] J. Wang, J. Wei, S. Su, J. Qiu, S. Wang, Ion-linked double-network hydrogel with high toughness and stiffness, *J. Mater. Sci.* 50 (2015) 5458–5465, <https://doi.org/10.1007/s10853-015-9091-0>.
- [59] Z. Wei, J.H. Yang, Z.Q. Liu, F. Xu, J.X. Zhou, M. Zrinyi, Y. Osada, Y.M. Chen, Novel biocompatible polysaccharide-based self-healing hydrogel, *Adv. Funct. Mater.* 25 (2015) 1352–1359, <https://doi.org/10.1002/adfm.201401502>.
- [60] X. Liu, X. He, D. Jin, S. Wu, H. Wang, M. Yin, A. Aldalbah, M. El-Newehy, X. Mo, J. Wu, A biodegradable multifunctional nanofibrous membrane for periodontal tissue regeneration, *Acta Biomater.* 108 (2020) 207–222, <https://doi.org/10.1016/j.actbio.2020.03.044>.
- [61] D. Kim, S. Lee, H. Kwon, J. Seo, Water resistance and antimicrobial properties of poly(vinyl alcohol) composite films containing surface-modified tetrapod zinc oxide whiskers, *Macromol. Res.* 23 (2015) 1134–1143, <https://doi.org/10.1007/s13233-015-3148-4>.
- [62] M. Godoy-Gallardo, U. Eckhard, L.M. Delgado, Y.J.D. de Roo Puente, M. Hoyos-Nogues, F.J. Gil, R.A. Perez, Antibacterial approaches in tissue engineering using metal ions and nanoparticles: from mechanisms to applications, *Bioact Mater* 6 (2021) 4470–4490, <https://doi.org/10.1016/j.bioactmat.2021.04.033>.
- [63] M.A. Rauf, M. Owais, R. Rajpoot, F. Ahmad, N. Khan, S. Zubair, Biomimetically synthesized ZnO nanoparticles attain potent antibacterial activity against less susceptible *S. aureus* skin infection in experimental animals, *RSC Adv.* 7 (2017) 36361–36373, <https://doi.org/10.1039/C7RA05040B>.
- [64] S. Safariarad, M. Mehrabi, B. Divband, M. Kosari-Nasab, Biofabrication of zinc oxide nanoparticles using fruit extract of Rosa canina and their toxic potential against bacteria: a mechanistic approach, *Mater. Sci. Eng. C Mater. Biol. Appl.* 59 (2016) 296–302, <https://doi.org/10.1016/j.msec.2015.09.089>.
- [65] K. Hantke, Bacterial zinc uptake and regulators, *Curr. Opin. Microbiol.* 8 (2005) 196–202, <https://doi.org/10.1016/j.mib.2005.02.001>.
- [66] B. Zhang, J. He, M. Shi, Y. Liang, B. Guo, Injectable self-healing supramolecular hydrogels with conductivity and photo-thermal antibacterial activity to enhance complete skin regeneration, *Chem. Eng. J.* 400 (2020), <https://doi.org/10.1016/j.cej.2020.125994>.
- [67] Z. Jamil, S.T.Q. Naqvi, S. Rasul, S.B. Hussain, N. Fatima, M.I. Qadir, S. A. Muhammad, Antibacterial activity and characterization of zinc oxide nanoparticles synthesized by microalgae, *Pak. J. Pharm. Sci.* 33 (2020) 2497–2504, <https://doi.org/10.36721/PJPS.2020.33.6.REG.2497-2504.1>.
- [68] M.A. Zia, M.K. Khosa, M. Muneer, K.M. Zia, M.J. Saif, Antimicrobial, selective antibiofilm, and antioxidant properties of plasticized PMMA/PVC and zinc oxide nano filler for biomedical applications, *Pak. J. Pharm. Sci.* 35 (2022) 233–238, <https://doi.org/10.36721/PJPS.2022.35.1.SUP.233-238.1>.
- [69] R. Augustine, H.N. Malik, D.K. Singhal, A. Mukherjee, D. Malakar, N. Kalarikkal, S. Thomas, Electrospun polycaprolactone/ZnO nanocomposite membranes as biomaterials with antibacterial and cell adhesion properties, *J. Polym. Res.* 21 (2014) 347, <https://doi.org/10.1007/s10965-013-0347-6>.
- [70] M. Shafiq, Y. Chen, R. Hashim, C. He, X. Mo, X. Zhou, Reactive oxygen species-based biomaterials for regenerative medicine and tissue engineering applications, *Front. Bioeng. Biotechnol.* 9 (2021), 821288, <https://doi.org/10.3389/fbioe.2021.821288>.
- [71] Y. Zhao, S. Song, D. Wang, H. Liu, J. Zhang, Z. Li, J. Wang, X. Ren, Y. Zhao, in: Nanozyme-reinforced Hydrogel as a H2O2-driven Oxygen generator for Enhancing Prosthetic Interface Osseointegration in Rheumatoid Arthritis Therapy 13, 2022, p. 6578, <https://doi.org/10.1038/s41467-022-34481-5>.
- [72] Y. Chen, W. Xu, M. Shafiq, D. Song, T. Wang, Z. Yuan, X. Xie, X. Yu, Y. Shen, B. Sun, Y. Liu, X. Mo, Injectable nanofiber microspheres modified with metal phonic networks for effective osteoarthritis treatment, *Acta Biomater.* (2022), <https://doi.org/10.1016/j.actbio.2022.11.040>.
- [73] R. Shi, H. Li, X. Jin, X. Huang, Z. Ou, X. Zhang, G. Luo, J. Deng, Promoting re-epithelialization in an oxidative diabetic wound microenvironment using self-assembly of a ROS-responsive polymer and P311 peptide micelles, *Acta Biomater.* 152 (2022) 425–439, <https://doi.org/10.1016/j.actbio.2022.09.017>.
- [74] M. Liu, X. Wang, J. Cui, H. Wang, B. Sun, J. Zhang, B. Rolaufts, M. Shafiq, X. Mo, Z. Zhu, J. Wu, Electrospun flexible magnesium-doped silica bioactive glass nanofiber membranes with anti-inflammatory and pro-angiogenic effects for infected wounds, *J. Mater. Chem. B* 11 (2023) 359–376.

- [75] Y. Chen, Z. Yuan, W. Sun, M. Shafiq, J. Zhu, J. Chen, H. Tang, L. Hu, W. Lin, Y. Zeng, Vascular endothelial growth factor-recruiting nanofiber bandages promote multifunctional skin regeneration via improved angiogenesis and immunomodulation, *Adv. Fiber. Mater.* (2022), <https://doi.org/10.1007/s42765-022-00226-8>.
- [76] J. Cui, X. Yu, Y. Shen, B. Sun, W. Guo, M. Liu, Y. Chen, L. Wang, X. Zhou, M. Shafiq, X. Mo, Recent advancements on inorganic electrospun nanofiber scaffolds for tissue engineering applications, *Nanomaterials* 13 (2023) 204, <https://doi.org/10.3390/nano13010204>.
- [77] J. Wang, Y. Cheng, L. Chen, T. Zhu, K. Ye, C. Jia, H. Wang, M. Zhu, C. Fan, X. Mo, In vitro and in vivo studies of electroactive reduced graphene oxide-modified nanofiber scaffolds for peripheral nerve regeneration, *Acta Biomater.* 84 (2019) 98–113, <https://doi.org/10.1016/j.actbio.2018.11.032>.
- [78] M. Kempf, Y. Miyamura, P.-Y. Liu, A.C.H. Chen, H. Nakamura, H. Shimizu, Y. Tabata, R.M. Kimble, J.R. McMillan, A denatured collagen microfiber scaffold seeded with human fibroblasts and keratinocytes for skin grafting, *Biomaterials* 32 (2011) 4782–4792, <https://doi.org/10.1016/j.biomaterials.2011.03.023>.
- [79] H. Sorg, D.J. Tilkorn, S. Hager, J. Hauser, U. Mirastschijski, Skin wound healing: an update on the current knowledge and concepts, *Eur. Surg. Res.* 58 (2017) 81–94, <https://doi.org/10.1159/000454919>.
- [80] E. Mariani, F. Mangialasche, F.T. Feliziani, R. Cechetti, M. Malavolta, P. Bastiani, M. Baglioni, G. Dedoussis, T. Fulop, G. Herbein, J. Jajte, D. Monti, L. Rink, E. Mocchegiani, P. Mecocci, Effects of zinc supplementation on antioxidant enzyme activities in healthy old subjects, *Exp. Gerontol.* 43 (2008) 445–451.
- [81] X. Zhang, D.M. Mosser, Macrophage activation by endogenous danger signals, *J. Pathol.* 214 (2008) 161–178, <https://doi.org/10.1016/j.exger.2007.10.012>.
- [82] H. Feng, I. Pyykko, J. Zou, Involvement of ubiquitin-editing protein A20 in modulating inflammation in rat cochlea associated with silver nanoparticle-induced cd68 upregulation and TLR4 activation, *Nanoscale Res. Lett.* 11 (2016) 240, <https://doi.org/10.1186/s11671-016-1430-9>.
- [83] Z. Wang, Y. Cui, J. Wang, X. Yang, Y. Wu, K. Wang, X. Gao, D. Li, Y. Li, X. Zheng, Y. Zhu, D. Kong, Q. Zhao, The effect of thick fibers and large pores of electrospun poly(ϵ -caprolactone) vascular grafts on macrophage polarization and arterial regeneration, *Biomaterials* 35 (2014) 5700–5710, <https://doi.org/10.1016/j.biomaterials.2014.03.078>.
- [84] Z. Feng, Q. Su, C. Zhang, P. Huang, H. Song, A. Dong, D. Kong, W. Wang, Bioinspired nanofibrous glycopeptide hydrogel dressing for accelerating wound healing: a cytokine-free, M2-type macrophage polarization approach, *Adv. Funct. Mater.* 30 (2020), 2006454, <https://doi.org/10.1002/adfm.202006454>.
- [85] M. Shafiq, S.H. Kim, Biomaterials for host cell recruitment and stem cell fate modulation for tissue regeneration: focus on neuropeptide substance P, *Macromol. Res.* 24 (2016) 951–960, <https://doi.org/10.1007/s13233-016-4134-1>.
- [86] C.J. Ferrante, S.J. Leibovich, Regulation of macrophage polarization and wound healing, *Adv. Wound Care* 1 (2012) 10–16, <https://doi.org/10.1089/wound.2011.0307>.
- [87] M. Shafiq, Y. Jung, S. Kim, Insight on stem cell preconditioning and instructive biomaterials to enhance cell adhesion, retention, and engraftment for tissue repair, *Biomaterials* 90 (2016) 85–115, <https://doi.org/10.1016/j.biomaterials.2016.03.020>.
- [88] A. Joshi, Z. Xu, Y. Ikegami, K. Yoshida, Y. Sakai, A. Joshi, T. Kaur, Y. Nakao, Y.-I. Yamashita, H. Baba, S. Aishima, N. Singhu, H. Ijima, Exploiting synergistic effect of externally loaded bFGF and endogenous growth factors for accelerated wound healing using heparin functionalized PCL/gelatin co-spun nanofibrous patches, *Chem. Eng. J.* 404 (2021), 126518, <https://doi.org/10.1016/j.cej.2020.126518>.